An immunogenic cell injury module for the single-cell multiplexed activity metabolomics platform to identify promising anti-cancer natural products

Received for publication, March 5, 2022, and in revised form, July 14, 2022 Published, Papers in Press, August 2, 2022,
https://doi.org/10.1016/j.jbc.2022.102300

Joseph A. Balsamo[1], Kathryn E. Penton[2], Zhihan Zhao[2], Madeline J. Hayes[3,4], Sierra M. Lima[3,4], Jonathan M. Irish[3,4,5,6], and Brian O. Bachmann[1,2,5,*]

From the [1]Department of Pharmacology, [2]Department of Chemistry, and [3]Department of Cell and Developmental Biology, Vanderbilt University, Nashville, Tennessee, USA; [4]Department of Pathology, Microbiology and Immunology, Vanderbilt University Medical Center, Nashville, Tennessee, USA; [5]Vanderbilt Institute of Chemical Biology, Nashville, Tennessee, USA; [6]Vanderbilt-Ingram Cancer Center, Vanderbilt University Medical Center, Nashville, Tennessee, USA

Edited by Donita Brady

Natural products constitute and significantly impact many current anti-cancer medical interventions. A subset of natural products induces injury processes in malignant cells that recruit and activate host immune cells to produce an adaptive anti-cancer immune response, a process known as immunogenic cell death. However, a challenge in the field is to delineate forms of cell death and injury that best promote durable antitumor immunity. Addressing this with a single-cell chemical biology natural product discovery platform, like multiplex activity metabolomics, would be especially valuable in human leukemia, where cancer cells are heterogeneous and may react differently to the same compounds. Herein, a new ten-color, fluorescent cell barcoding-compatible module measuring six immunogenic cell injury signaling readouts are as follows: DNA damage response (γH2AX), apoptosis (cCAS3), necroptosis (p-MLKL), mitosis (p-Histone H3), autophagy (LC3), and the unfolded protein response (p-EIF2α). A proof-of-concept screen was performed to validate functional changes in single cells induced by secondary metabolites with known mechanisms within bacterial extracts. This assay was then applied in multiplexed activity metabolomics to reveal an unexpected mammalian cell injury profile induced by the natural product narbomycin. Finally, the functional consequences of injury pathways on immunogenicity were compared with three canonical assays for immunogenic hallmarks, ATP, HMGB1, and calreticulin, to correlate secondary metabolite-induced cell injury profiles with canonical markers of immunogenic cell death. In total, this work demonstrated a new phenotypic screen for discovery of natural products that modulate injury response pathways that can contribute to cancer immunogenicity.

Small molecule anti-cancer agents are typically discovered *via* high-throughput target-based approaches or untargeted cytotoxicity screens that reflect essential cellular processes such as DNA replication, cytoskeletal remodeling, or metabolism. Compounds from both discovery paradigms are well represented in the clinic by synthetic compounds and natural products (1). For example, imatinib is a synthetic drug developed to treat chronic myelogenous leukemia that blocks nucleotide triphosphate–binding pockets of tyrosine kinases, notably BCR/ABL, to stabilize inactive state complexes and prevent downstream signaling (2). The natural products anthracyclines and taxanes, initially discovered *via* cytotoxicity assays, were later observed to interfere with DNA replication and microtubule stability, respectively (3, 4). Imatinib, anthracyclines, and taxanes are all featured in the World Health Organization's list of essential medicines, underlining the complementarity of target-based and phenotypic discovery modes (5).

In addition to tumor toxicity, some chemotherapeutics are thought to be effective because they trigger immunogenic cell death (ICD). ICD is a property of moribund cells that elicits inflammation toward a therapeutically productive adaptive antitumor immune response (6, 7). Notably, combining inflammatory agents that induce ICD with checkpoint blockade therapy enhanced survival in animal models (8–12). Examples of studied ICD inducers include widely prescribed chemotherapies, such as the anthracycline daunorubicin, peptide actinomycin D, podophyllotoxin teniposide, and platinum-based antineoplastic oxaliplatin (6, 13–16). ICD can activate both innate and adaptive immune responses *via* expression of damage associated molecular patterns (DAMPs) including secretion of ATP, release of nuclear protein HMGB1, and surface exposure of endoplasmic reticulum resident protein calreticulin (eCRT) to name a few (17). These immunogenic DAMPs comprise 'find me' and 'eat me' signals that trigger recruitment and activation of antigen presenting cells, such as dendritic cells and macrophages, that initiate antigen-specific immune responses (17).

Recently, the phenomenon of chemically induced antitumor immunity has broadened to include living cells. In these processes, live injured cells facilitate innate and adaptive immunity (11, 18, 19) independent of canonical ICD hallmarks (12), suggesting that additional modes of immunogenic induction

* For correspondence: Brian O. Bachmann, brian.bachmann@vanderbilt.edu.

remain to be discovered. Herein, the term "immunogenic cell injury" (ICI) refers to all types of immunogenic injury responses in injured or dying cancer cells. Based on these and prior studies (20–22), it is apparent that the various forms of chemically induced cell death and injury do not yield comparable immunogenic responses. There is a gap in understanding how cell death and injury pathways connect to the display of DAMPs that elicit therapeutically productive immune responses. Thus, we developed an injury cytometric module composed of fluorescent antibodies that detect molecular injury and stress markers.

To expedite the discovery of immunogenic small molecule therapies, the injury module was designed with benchmark secondary metabolites that elicit injury phenotypes (Table S1). The topoisomerase poison etoposide effects DNA double strand breaks detected by phosphorylation of H2AX variant at serine 139 (γH2AX) (23, 24) and can act as an adjuvant signal to immunogenicity (12). The pan-kinase alkaloid inhibitor staurosporine, a potent apoptotic agent (25, 26), prompts cleavage of the caspase-3 zymogen to its active form (cCAS3) (27). Apoptotic activation is required for doxorubicin-induced immunogenicity (6). Likewise, autophagy and the unfolded protein response are critical injuries for assessing immunogenic potential because they are required for ICD (10, 28). The autophagy marker LC3 or unfolded protein response (UPR) marker p-EIF2α are specifically inducible with the vacuolar H^+-ATPase (v-ATPase) inhibitor bafilomycin (29–31) or SERCA inhibitor thapsigargin, respectively (32–34). Additionally, an explosive form of cell death known as necroptosis has gained traction as an immunogenic signal that is dependent on the RIPK–MLKL signaling pathway that is marked by phosphorylation of MLKL at serine 358 (p-MLKL) (35–37). The benzimidazole natural product–inspired molecule nocodazole disrupts microtubule dynamic instability (38) that enables intracellular detection of p-MLKL (39) and inhibits M-phase measured by expression of phosphorylated histone H3 at serine 28 (p-HH3) (Table S1) (27).

Following compound selection, each injury was assigned to a fluorescent channel that was compatible with fluorescent cell barcoding (FCB), to enhance sample throughput, and validated on next generation spectral flow cytometers, to broaden detection of molecular injury signals. The completed injury module was applied to aid identification of natural products that bias signaling pathways toward an immunogenic fate. The benchmark bioactive secondary metabolites (Table S1) were evaluated with multiplexed activity profiling (MAP) to identify optimal dose and timing for cell death and injury pathways preceding ICI-mediated DAMP induction (40–43) and then correlated to immunogenic hallmarks calreticulin, ATP, and HMGB1 by principal component analysis. A multiplexed activity metabolomics (MAM) approach was used to test a discovery workflow that matched bioactivity of fractioned extracts to potentially immunogenic compounds by correlating secondary metabolome mass spectra with single cell fluorescent cytometry data. The compounds bafilomycin A1, staurosporine, and nocodazole were spiked into an inert metabolomic extract and fractioned into plate wells. Despite the presence of contaminating lipids, primary metabolites, and other fermentation products, bioactivity was only observed in fractions containing benchmark compounds, demonstrating the specific and sensitive detection of chemically induced cell injury with this injury module. Following successful validation, the module was applied using MAP and MAM workflows to identify bioactive metabolites in five untested microbial extracts generated from cave-sourced actinomycetes. This resulted in the discovery of an unexpected injury response profile of the secondary metabolite narbomycin (44).

The ICI module coupled with FCB and viability stain established a ten-color (six ICI functional markers, one viability marker, and three barcoding dye) flow cytometry panel that performed 336 individual assays per flow cytometry run (seven functional markers across 48 plate wells). Secondary assays measured the expression of known immunogenic DAMPs: ATP, HMGB1, and eCRT. Assessing injury patterns in microtiter wells with millions of individual cells and comparing them to well-characterized benchmark injury control compounds provided insights into the connection among immunogenic signals and afforded a discovery platform for compounds that induce ICI hallmarks.

Results

Antibody validation for detection of compounds that enhance UPR and necroptotic markers

To validate injury-specific antibodies for the ICI module, chemical induction was used to measure injury phenotypes following 10 μM challenge for 24 h in fixed cells with a five-color panel (Fig. 1*A*). Vehicle-treated cells served as negative controls and were labeled with Alexa 750 (A × 750) fluorescent dye. Etoposide-treated cells were included as a positive control for chemical-specific induction of DNA damage response sensor γH2AX and labeled with Pacific Orange fluorescent dye (Fig. 1*A*). The γH2AX signal was detected with a fluorescently conjugated mouse primary antibody (Table S2). Cell populations challenged with the terpenoid thapsigargin or benzimidazole derivative nocodazole were stained independently with Pacific Blue dye and evaluated for UPR and necroptotic signal induction, respectively (10, 39, 45, 46).

Commercially available flow cytometry–validated antibodies for these ICI signals were unavailable, thus antibodies applied in other techniques (Table S1) were utilized to observe chemically induced injury signals. These two markers were targeted with phospho-specific unconjugated rabbit primary antibodies and detected with a fluorescent goat secondary antibody specific to rabbit Fc IgG (Fig. 1*A* and Table S2). Separate thapsigargin- or nocodazole-challenged cell populations were mixed with etoposide and vehicle-challenged cells and stained for the ICI marker of interest for detection with a spectral flow cytometer. Cells were gated as viable-singlets and isolated from drug challenged populations by their fluorescent dye label (Figs. 1*B* and S1, Experimental procedures). Thapsigargin- and nocodazole-challenged cells exhibited a right-shifted cell population that was quantified as percent in gate for positive secondary fluorescent antibody

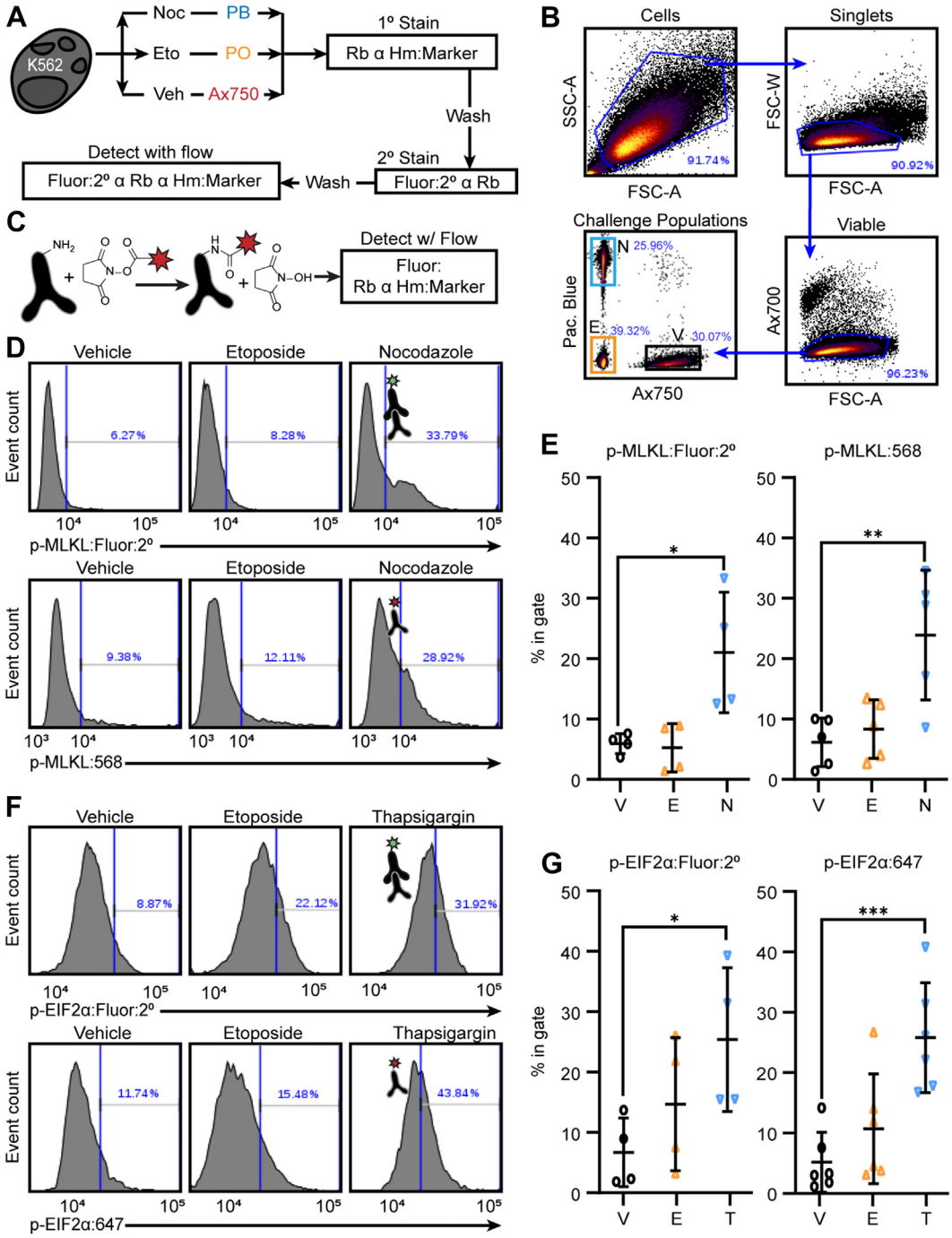

Figure 1. Antibody validation by detection of chemically induced cell injury. *A*, experimental scheme that measured chemically induced cell phenotypes by color-coded challenge conditions with a marker-specific rabbit primary antibody and a fluorescent goat secondary antibody. *B*, gating strategy for signal deconvolution to assess challenge-specific cell responses. Cells were treated for 24 h with 10 μM nocodazole or etoposide and vehicle control and then viability stained, fixed, permeabilized, and fluorescently labeled with NHS-functionalized fluorescent dyes: nocodazole - *Pacific Blue* - *Blue Box*, etoposide - *Pacific Orange* - *Orange Box*, Vehicle - A × 750 - *Black Box*. Viable-singlet cells were isolated to compound-specific populations by matched fluorescent signal to distinguish chemically induced cell phenotypes. *C*, conjugation reaction of NHS-functionalized fluorescent dyes to antibody primary amines. *D*, representative cell count histograms of p-MLKL detection with a fluorescent secondary antibody (*top*) and p-MLKL conjugated to A × 568 (*bottom*). *E*, scatter plots show chemically induced injury as percent in gate mean ± S.D (n = 4, one-way ANOVA with Dunnett's multiple comparisons test) of p-MLKL detection with fluorescent secondary (*left*) or p-MLKL:568 (*right*). *F*, procedure in (*A–C*) were repeated for p-EIF2α–directed antibody with the exception of natural product (thapsigargin) and conjugate fluorophore (A × 647). Representative cell count histograms of p-EIF2α detection with a fluorescent secondary antibody (*top*) and p-EIF2α conjugated to A × 647 (*bottom*). *G*, scatter plots show chemically induced fluorescent signal measured as percent in gate mean ± S.D (n = 6, One-way ANOVA with Dunnett's multiple comparisons test) of p-EIF2α detection with fluorescent secondary (*left*) or p-EIF2α:647 (*right*). $p <$ **0.05, **0.01, *** 0.001*; V, vehicle; E, etoposide; N, nocodazole; T, thapsigargin; NHS, N-hydroxy succinimide.

signal and compared to etoposide and vehicle controls with one-way ANOVA (Fig. 1, *D–G*). Positive signal was also compared to a fluorescent secondary control that was absent of primary antibody to confirm measured biological responses was not due to nonspecific binding of the fluorescent goat secondary antibody (Fig. S2 and Table S1). Neither etoposide

nor vehicle activated UPR or necroptotic injury signals (Fig. 1, *D*–*G*). Moreover, etoposide-treated cells were γH2AX positive, while γH2AX levels in thapsigargin- and nocodazole-challenged populations remained unchanged (Fig. S3). The detection of chemically induced p-EIF2α and p-MLKL validated these antibodies for flow cytometry applications.

Next, the two validated ICI flow antibodies required fluorescent functionalization and confirmation that fluorescent modifications did not abolish target binding. Antibodies targeting p-EIF2α and p-MLKL were fluorescently conjugated with covalent primary amine reactive Alexa Fluor dyes (Fig. 1*C*, Experimental procedures). Conjugation intensity was evaluated by fluorescence SDS-PAGE under reducing and nonreducing conditions and exhibited fluorescent signal at molecular weights of 150 kDa, 50 kDa, and 25 kDa consistent with full length, heavy chain, and light chain rabbit antibody molecular weights (Fig. S4). Detection of p-EIF2α and p-MLKL were repeated as described above and confirmed covalent modifications of antibodies did not negatively affect target binding (Fig. 1, *D*–*G*).

MAP rapidly screens for injury responses in leukemia cell lines

Validated ICI module antibodies were then applied to a MAP workflow to rapidly screen three leukemia cell lines to identify adequate concentrations and challenge times for reliable ICI induction (Fig. 2*A*) with the compounds bafilomycin A1, etoposide, nocodazole, staurosporine, and thapsigargin (Table S1) (27, 29, 31, 46). Leukemia model cell lines K562 (chronic myelogenous leukemia), MV-4-11 (B-myelomonocytic leukemia), and Jurkat (T cell leukemia) cells were challenged with 10 μM, 1 μM, 0.1 μM, and 0.01 μM of each compound for 4, 24, and 48 h (Fig. 2*A*). At each timepoint, cells were fixed, permeabilized, fluorescently barcoded, and stained with the ICI module for flow cytometry (Fig. 2*A*). Following data acquisition, samples were quality control gated and debarcoded (Figs. 2, *B* and *C* and S5). Each leukemia cell line exhibited unique injury profiles to each challenge condition over time (Figs. 2*C* and S5) and thus evaluated for the clearest marker responses.

Autophagy marker LC3 is reliably induced by bafilomycin A1 in leukemia models

The three tested leukemia cell lines were all sensitive to LC3 induction by the nanomolar v-ATPase inhibitor bafilomycin A1 across timepoints and concentrations consistent with previous reports (31–33). MV-4-11 was sensitive to LC3 expression by all compounds at all doses, except for 10 nM nocodazole after 48-h challenge (Fig. S5). LC3 levels in Jurkat were less pronounced but present in bafilomycin A1 and etoposide treatment conditions (Fig. S5). The K562 cell line also demonstrated autophagic marker induction, most prominently in bafilomycin A1 challenge conditions (Fig. 2*C*). Unlike MV-4-11 and Jurkat,

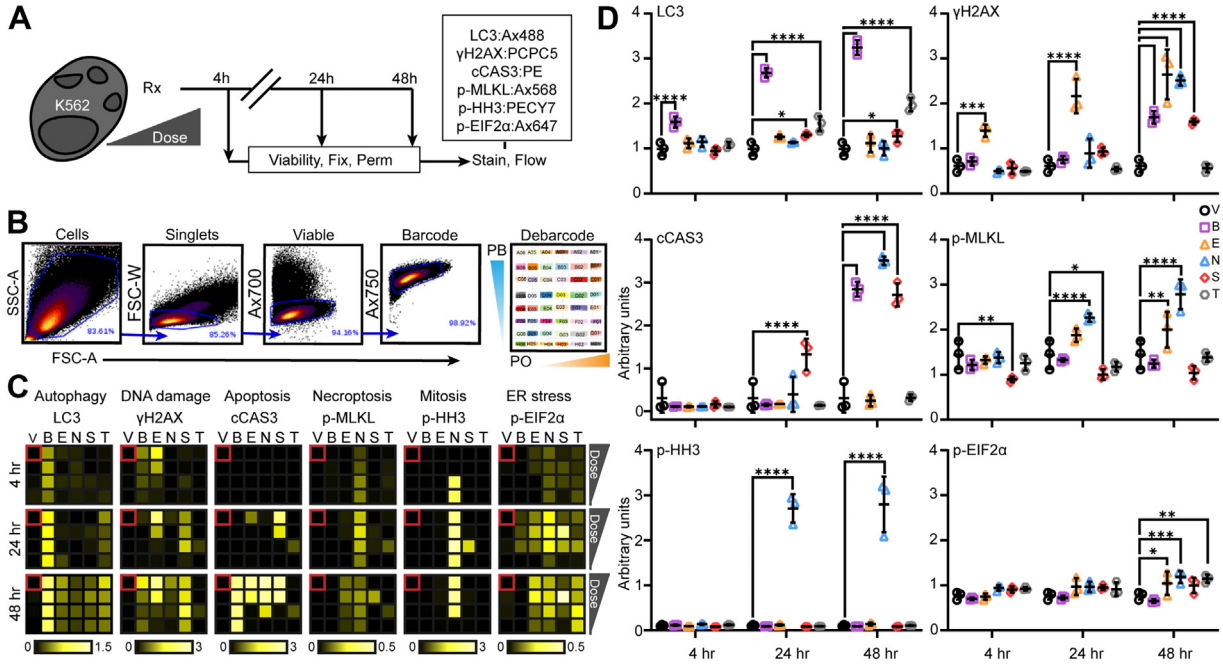

Figure 2. Multiplexed activity profiling of cell injury across dose and time. *A*, K562 cells were dosed with six compounds from 10 μM to 10 nM by ten-fold serial dilution. Each timepoint, 4, 24, and 48 h, were viability stained, fixed, permeabilized, and fluorescently barcoded. Sets of 48 barcoded wells were pooled by timepoint and then stained with a fluorescent antibody cocktail to measure individual well responses to each fluorescent injury signal simultaneously with flow cytometry. *B*, cells were gated as viable-singlets stained with NHS-functionalized A × 750 cell uptake control dye. Cells were then debarcoded and digitally reassigned to origin wells to assess well-by-well marker responses (LC3, apoptosis; γH2AX, DNA damage; cCAS3, apoptosis; p-MLKL, necroptosis; p-HH3, M-phase; p-EIF2α, UPR). *C*, multiplexed activity profiling of injury signals induced by small molecules is represented by a heat map of the 95th percentile of the arcsinh ratio to vehicle control well outlined in *red*. *D*, compound-specific, time-dependent injury at 1 μM challenge revealed nascent temporal relationships among injury phenotypes imposed by secondary metabolites with specific mechanisms of action. Scatter plots show raw 95th percentile of fluorescent marker intensity as mean ± S.D and tested for significance against vehicle control of respective timepoints (n = 3, two-way ANOVA with Dunnett's multiple comparison's test). $p <$ *0.05, **<0.01, ***<0.001, ****<0.0001; V, vehicle; B, bafilomycin A1; E, etoposide; N, nocodazole; S, staurosporine; T, thapsigargin; PB, Pacific Blue; PO, Pacific Orange; NHS, N-hydroxy succinimide.

K562 cells did not exhibit elevation of autophagy marker LC3 *via* off-target compounds or signaling cross talk but rather remained largely restricted to induction by bafilomycin A1 inhibition of v-ATPase (Figs. 2*C* and S5).

Since K562 cells best conserved on-target signal specificity over time, they were subjected to additional testing to confirm positive assay performance. Challenge with 1 μM bafilomycin A1 significantly elevated LC3 levels in 4 h and continued signal elevation through 24- and 48-h timepoints (Fig. 2*D*). Additionally, 1 μM thapsigargin increased LC3 after 24- and 48-h challenge. The thapsigargin-induced LC3 phenotype is potentially due to increased autophagy to compensate for enduring ER strain (Fig. 2*D*) (39), whereas bafilomycin A1–enhanced LC3 are due to blocked acidification of LC3-associated autophagic compartments that prevents LC3 degradation (29, 30). Thus, positive LC3 signal of unknown compounds may be attributed to activation or inhibition of autophagy and require deeper molecular investigation.

Staurosporine and thapsigargin challenge also increased LC3 injury signal at 24 and 48 h, while etoposide and nocodazole did not elicit a response (Fig. 2*D*). The results in Figure 2*D* confirmed that bafilomycin A1 induced LC3 phenotype observed in Figure 2*C* and supported staurosporine and thapsigargin signal observed at 1 uM dose at 48 h (Fig. 2, *C* and *D*). Etoposide and nocodazole did not induce LC3 at 1 μM challenge over 48 h, suggesting the heat map signal intensity in Figure 2*C* was not biologically significant (Fig. 2*D*).

DNA damage is triggered by direct and indirect molecular mechanisms

Jurkat γH2AX expression was most notable in etoposide and staurosporine treatments at 4 h with apparent decrease by 48 h (Fig. S5). A similar phenomenon was observed in MV-4-11 cells (Fig. S5). K562 cells presented a direct DNA damage response over time when challenged with 10 μM and 1 μM of the topoisomerase inhibitor etoposide and also responded indirectly to staurosporine in a dose-dependent fashion that increased marker response from 24 to 48 h (Fig. 2*C*). The K562 DNA damage phenotype that was maintained through 48 h was confirmed with a 1 μM challenge over 48 h (Fig. 2*D*). Etoposide successfully induced DNA damage at all timepoints (Fig. 2*D*). Additionally, enhanced γH2AX levels were observed with non-DNA damaging bafilomycin A1, nocodazole, and staurosporine following 48-h challenge. This suggested that autophagy inhibition, disrupted dynamic instability, and prolonged kinase blockade can yield double stranded breaks *via* indirect molecular mechanisms over 48 h (Fig. 2, *C* and *D*).

Apoptosis can be elicited by prolonged secondary metabolite challenge

Jurkat and MV-4-11 cells were sensitive to cCAS3 induction at 4 h by all compounds, particularly staurosporine and thapsigargin at nanomolar concentrations (Fig. S5). Increased sensitivity to apoptotic induction over 48 h resulted in diminished cCAS3 activity as an artifact of viable cell loss by gating (Fig. 2*B*) rather than stress resolution (Fig. S5). The K562 cells manifested a staurosporine-specific cCAS3 phenotype in response to dose at 24 h and maintained this phenotype through 48 h (Fig. 2*C*). At 48 h, bafilomycin A1, etoposide, and nocodazole initiated cCAS3 response suggesting prolonged cellular stress of autophagy, DNA double strand breaks, or microtubule disruption can engage the apoptotic death effector pathway in K562 cell model (Fig. 2*C*). Due to the staurosporine-specific cCAS3 phenotype observed at 24 h and overall resilience to enduring chemical challenge accompanied by a cCAS3 phenotype (Fig. 2*C*), the K562 line was subjected to 1 μM time course to confirm MAP screening results. The pan-kinase inhibitor staurosporine increased cCAS3 signal to biologically significant levels at 24 and 48 h (Fig. 2*D*). Bafilomycin A1 and nocodazole cCAS3 induction was also apparent by 48 h keeping with initial screening data (Fig. 2*D*) and suggested extended induction with secondary metabolites may reveal additional proapoptotic chemical agents with bio-orthogonal molecular targets.

Necroptotic marker p-MLKL is sensitive to induction by nocodazole

Nocodazole-incubated K562 cells displayed increased levels of the necroptotic effector p-MLKL across timepoints and doses (Fig. 2*C*). The necroptotic marker p-MLKL was increased by nocodazole challenge at 24 h and 48 h (Fig. 2*D*) in line with validation (Fig. 1, *D* and *E*) and initial screening (Fig. 2*C*). Etoposide also stimulated p-MLKL presentation following 48-h challenge (Fig. 2*D*). It is important to consider nocodazole-challenged cells with enhanced p-MLKL is likely not necroptotic death but rather an accumulation of intracellular p-MLKL that fails to translocate from the nucleus to other cellular compartments over time due to nocodazole-altered microtubule dynamic instability (38, 47). Notably, staurosporine inhibited p-MLKL signal at 4 and 24 h with signal recovery by 48 h (Fig. 3*D*), which may be the result of cross talk between apoptotic and necroptotic signaling pathways (48, 49). Jurkat and MV-4-11 were more sensitive to induction of apoptotic effector cCAS3 than necroptotic effector p-MLKL (Fig. S5) and reflect cell type–specific responses with respect to leukemia subtypes.

The unfolded protein response signal is induced by thapsigargin and nocodazole

The UPR marker p-EIF2α was activated in K562 cells by thapsigargin consistent with reported SERCA inhibition (32–34), while Jurkat and MV-4-11 cells remained unresponsive and inconsistent with dosing (Figs. 2*C* and S5). In line with Figure 1 validation data and Figure 2 screening data, 1 μM thapsigargin induced p-EIF2α after 48-h challenge in K562 (Fig. 2*D*). Nocodazole and etoposide also increased UPR marker p-EIF2α to statistically significant values in 48-h challenge conditions (Fig. 2*D*). The observed p-EIF2α activation phenotype in nocodazole-treated cells was unexpected and not previously reported, thus nocodazole challenge was repeated as in Figure 1 to confirm nocodazole does impart a statistically significant increase in p-EIF2α in K562 (Fig. S6). It is also worth

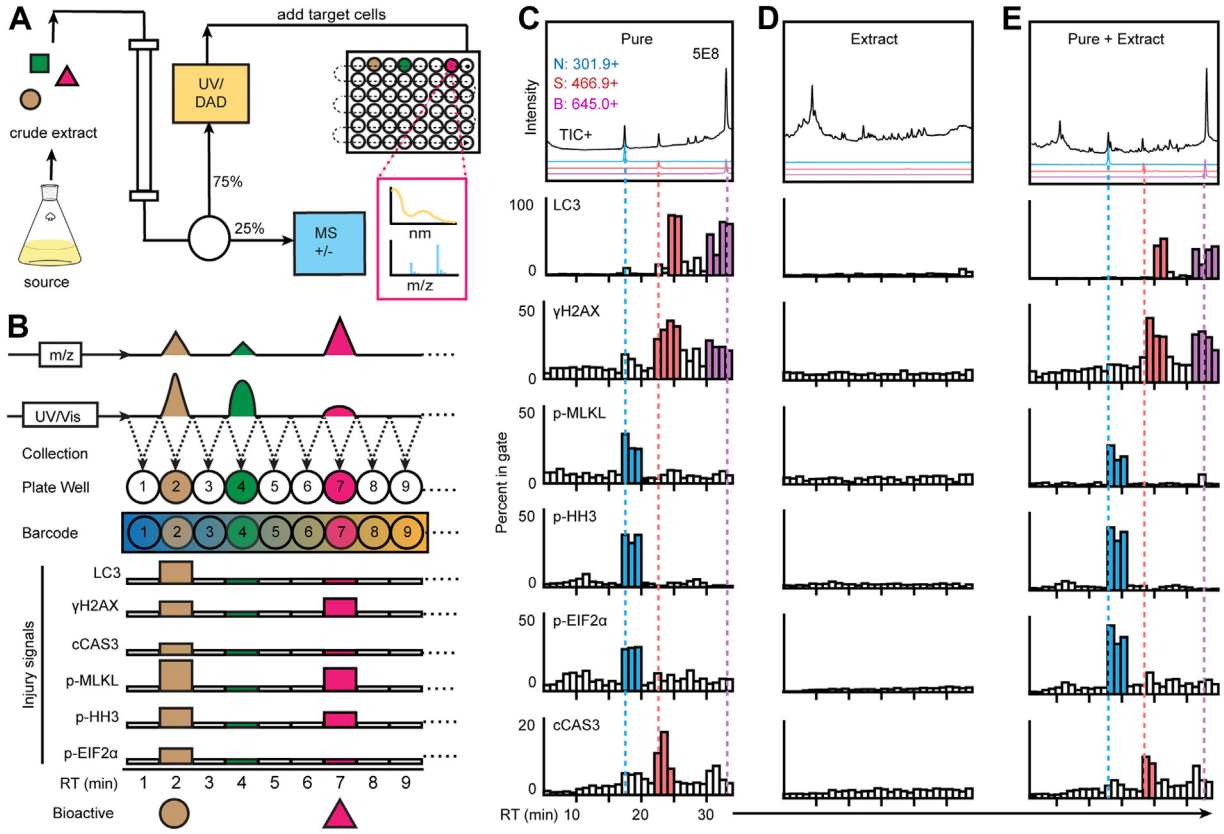

Figure 3. Multiplexed activity metabolomics aligns bioactivity with mass spectra. *A*, fractionation of crude metabolomic extracts by reverse phase, split flow HPLC/UV/MS with polarity switching mass scanning to associate metabolite spectral data to well eluates by retention time. Collected metabolomic fractions were lyophilized and plated under cell containing culture media. *B*, cells were fluorescently barcoded to origin wells, pooled, and stained with fluorescent antibody cocktail. Barcode and biological signal were detected for all wells simultaneously by flow cytometry. Cells were debarcoded to original well positions and evaluated for well-specific signal. *C*, pure compounds induced bioactive signal in plate wells aligned to mass spectra by retention time. *D*, an inert extract displays no significant bioactivity. *E*, proof of principle signal detection of pure, known bioactive components on inert metabolomic sample. Pure compounds mixed with inert extract in (*D*) exerted bioactivity in wells containing known compounds and repeated bioactivity of pure compounds shown in (*C*). Positive ion currents and correlated well activity is distinguished by color. N, nocodazole (*m/z*,301.9 $[M + 1]^+$), *blue*. S, staurosporine (*m/z* 466.9 $[M + 1]^+$), *red*. B, bafilomycin A1 (*m/z* 645.0 $[M + 1]^+$), *purple*.

noting that bafilomycin A1 promoted LC3 and failed to enhance p-EIF2α in contrast to thapsigargin-activating p-EIF2α and LC3. This observation further supports that ER strain may indirectly activate autophagy to compensate for cellular energetic requirements and that the UPR is unresponsive to autophagy inhibition in this model system (Fig. 2*D*).

In all, barcoded MAP screening provided a high-throughput and robust format for confirming panel fidelity and identification of chemically sensitive cell lines. The initial MAP screen in Figures 2*C* and S5 indicated that Jurkat and MV-4-11 were more sensitive to injury by inhibition of molecular targets outside canonical signaling pathways (*e.g.*, thapsigargin-activated cCAS3 in Fig. S5). K562, however, first activated injury signals consistent with molecular inhibition of specific targets prior to exhibiting off-target injury phenotypes (Fig. 2, *C* and *D*). The consistency and reliability of chemically induced K562 injury signals offered a model for unraveling ICI biomarker relationships to ICD signals in leukemia models.

MAM aligns injury phenotypes to bioactive compounds

The MAM discovery workflow system overlays multiplexed single cell chemical biological measurements onto characterized metabolomic arrays. Metabolomic extracts were chromatographically fractionated by high performance liquid chromatography. One part of the eluate was diverted to a mass spectrometric analyzer, and three parts were diverted to a UV/Vis diode array detector and collected in 96-well microtiter plates. Each plate well contained one-minute fractions of eluate that corresponded to retention times of collected MS/UV/Vis spectra (Fig. 3*A*). Fractioned metabolomes were dried *in vacuo*, resuspended with 1 μl dimethylsulfoxide (DMSO) and 200 μl culture media with a density of 1 million cells/ml, and incubated at 37 °C. Each well population was fixed, permeabilized, fluorescently barcoded, pooled, stained with the fluorescent ICI module, and acquired on a Cytek spectral flow cytometer for downstream analysis of biological signal. Microtiter plate wells with bioactivity were compared to corresponding mass spectra to identify potentially bioactive metabolite(s) by correlation of extracted ion negative and/or positive electrospray *m/z* and UV/VIS peaks with immunoassay trends (Fig. 3*B*).

To test for specific activity of ICI markers with MAM, individual chromatographic runs of injury control compounds were generated for etoposide, nocodazole, staurosporine, and bafilomycin A1 to verify separation into unique wells such that

ICI signals were attributed to only one spiked compound (Fig. S7). Thapsigargin was excluded from MAM due to its elution proximity to etoposide (Fig. S7) and because it displayed modest injury signals in MAP conditions (Fig. 2*D*). Bafilomycin A1, nocodazole, and staurosporine were selected for the positive control array since each compound eluted into a separate well (Figs. 3*C* and S7). K562 cells were incubated with the positive control array for 48 h and investigated for injury signal as percent positive cells in gate (Fig. 3*C*). Each MAM experiment included positive control wells containing pure control compounds as a reference for 'hit' bioactivity in addition to vehicle negative controls (Fig. S8). The positive extracted ion currents for nocodazole (*m/z* 301.9, $[M + H]^+$), staurosporine (*m/z* 466.9, $[M + H]^+$), and bafilomycin A1 (*m/z* 645.0, $[M + H]^+$) produced peaks with retention times that aligned to wells positive for fluorescent functional marker signal (Fig. 3*C*). Nocodazole-positive wells showed induction of p-MLKL, p-HH3, and p-EIF2α but not cCAS3 nor γH2AX (Fig. 3*C*). Staurosporine elution corresponded to an elevated cCAS3 signature along with γH2AX and LC3 consistent with observations in Figure 3*C*. However, maximal staurosporine-induced LC3 marker response did not precisely correlate with cCAS3 signal but rather occurred in wells immediately following. Thus, wells 22 to 27 were investigated for single cell responses for cCAS3 and LC3 simultaneously to evaluate marker signal at 48 h (Fig. S9). The elution peak, and thus highest concentrations of staurosporine, was split between wells 23 and 24, then diminished, and thus decreased in concentration, from wells 25 to 27. These observations were consistent with marker responses in Figure 2. Concentrations of staurosporine in excess of 1 μM rapidly induced cCAS3 without a corresponding LC3 signal (Fig. 2*C*), and LC3 injury is present after 48 h in sub-1 μM concentrations. Bafilomycin A1–containing wells were positive for LC3 and γH2AX consistent with Figure 2 (Fig. 3*C*).

The success of MAM depends on high-fidelity fluorescent cell status marker responses to bioactive components in the presence of potentially interfering primary metabolites, cell wall, membrane, and spent growth media components in typical microbial extracts. Thus, five extracts of various actinomycete genera were cultured in ISP2 and evaluated for apoptosis and DNA damage by serial dilution in the MV-4-11 cell line (Fig. S10). The KPBlue17 (99% 16S identity *Streptomyces exfoliatus*, NRRL B-2024) extract induced cCAS3 and γH2AX markers at all challenge doses (Fig. S10). Extract KPBlue22 (99% 16S identity *Streptomyces xantholiticus*, NBRC 13354) demonstrated single cell signal shifts for DNA damage response, γH2AX, at the highest dose of 0.63 mg/ml and failed to induce a cCAS3 response (Fig. S10). Several inert extracts exhibited in Fig. S10 did not increase observed injury markers regardless of dose. The inert extract KPBlue13 (99% 16S identity *Streptomyces pratensis*, NRRL B-24916) was arbitrarily selected from tested inactive extracts to confirm the ICI module for application using MAM (Fig. S10). Two metabolomic arrays were generated for evaluation (1): fractioned KPBlue13 and (2) fractioned KPBlue13 spiked with bafilomycin A1, nocodazole, and staurosporine (Fig. 3, *D* and *E*). The metabolomic array generated from the crude extract induced no significant marker changes in K562 cells (Fig. 3*D*), indicating minimal interference from media or cell-associated metabolites in the extract and conservation of negative activity between leukemia cell lines. The spiked extract, however, demonstrated marker shifts in K562 cells matched to bafilomycin A1-, nocodazole-, and staurosporine-containing wells that aligned to retention times of their respective extracted ion currents (Fig. 3*E*). The specific activity observed in the spiked MAM were consistent with injury control compound retention times and mirrored results from pure injury control injections (Fig. 3, *C* and *E*). Taken together, this data demonstrated a robust system for high-throughput and simultaneous identification of bioactive metabolite-associated *m/z* features within a chemically complex metabolome that impact a diverse array of terminal stress effectors.

MAM identifies novel activity of the secondary metabolite narbomycin in an unknown extract

The hypogean *Streptomyces* KPBlue17 demonstrated bioactivity across all serial dilutions at concentrations as low as 0.04 mg/ml in MV-4-11 and K562 cell lines (Figs. S10 and S11). Conservation of activity at these dilutions predicted sufficient specific activity to facilitate identification of a metabolite using MAM. Therefore, the extract was subjected to MAM and evaluated for activity at 24 and 48 h. Enhanced marker shifts for autophagy, DNA damage, and apoptosis were observed in well 24, which aligned to a positive ion peak with an extracted current of *m/z* 509.7 $[M + H]^+$ (Fig. 4, *A* and *B*). The isolation of the activity correlated peak was prioritized and preliminarily identified to be the macrolide antibiotic narbomycin by *m/z* (Fig. 4*C*) and subsequently confirmed by NMR (^{1}H and HSQC, Figs. S12 and S13) and comparison to literature data (44). Injury signals in narbomycin-containing wells increased from 24 to 48 h *via* prolonged exposure to the bioactive agent (Fig. 4*D*). All other wells remained inactive (Fig. 4*D*). The narbomycin-induced injury phenotype is consistent with studies of other ribosome-binding members of the macrolide family of natural products, including azithromycin and clarithromycin, that are reported inhibitors of autophagic flux and capable of modulating apoptotic responses (50–52). The induction of DNA damage response marker γH2AX by narbomycin has never been reported and is not well documented overall in macrolides.

Detection of immunogenic hallmarks in a leukemia cell line

Following application of the cell injury module, the relationships between chemically induced cell injury to reported immunogenic DAMPs were investigated, namely ATP, HMGB1, and eCRT. Injury control compounds were used to challenge K562 cells to evaluate extracellular release of ATP and HMGB1 to the cell supernatant and eCRT on the cell surface (Fig. 5*A*). Extracellular ATP release was first observed at 24 h by the autophagy inhibitor bafilomycin A1 (Fig. 5*B*). This persisted to 48 h and more than doubled extracellular ATP concentrations (Fig. 5*B*). Pan-kinase inhibition by

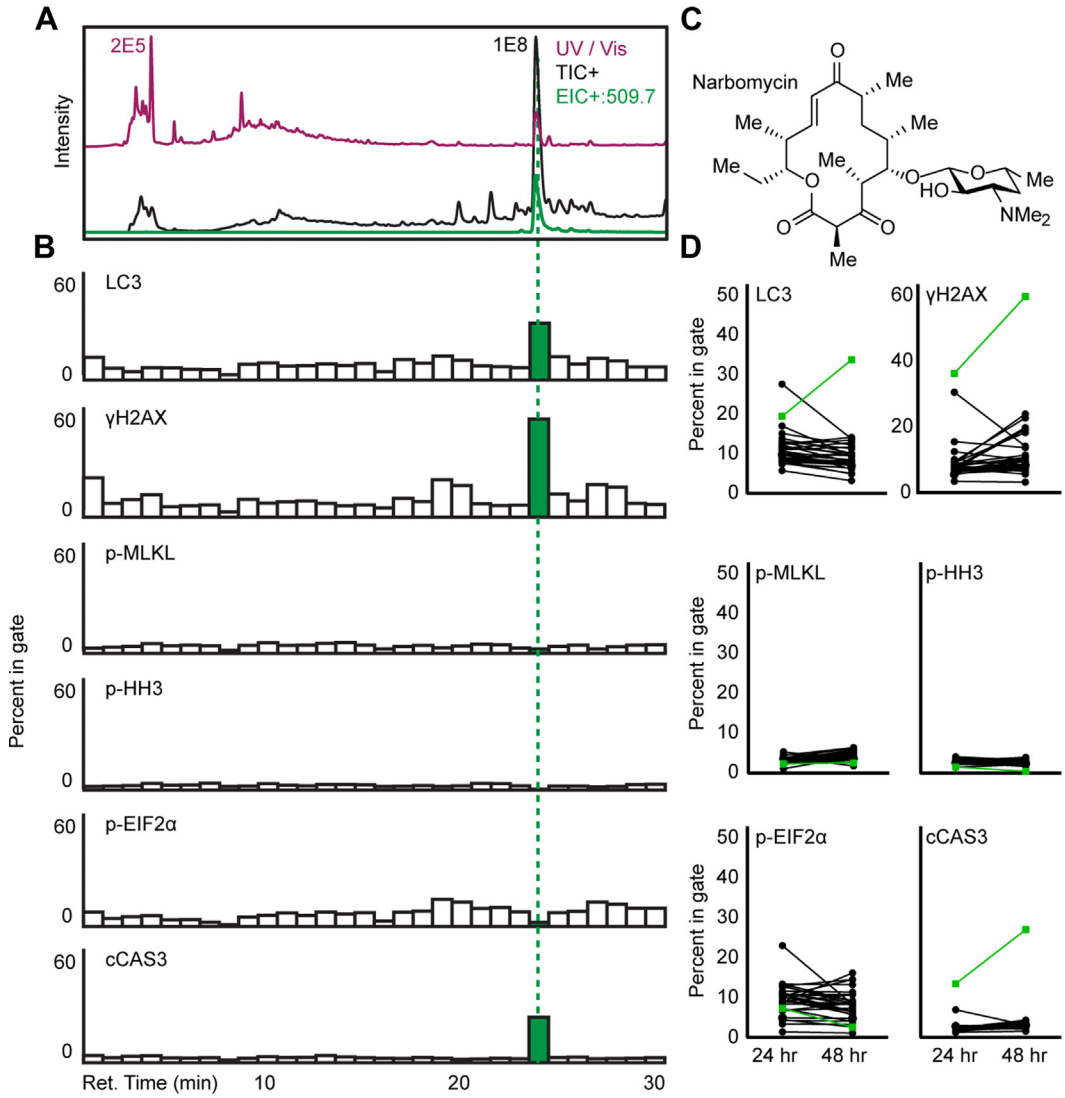

Figure 4. Multiplexed activity metabolomics informs isolation of secondary metabolites by injury signatures. *A*, KPBlue17 crude extract was fractioned by reverse phase, split flow HPLC/UV/MS with polarity switching mass scanning to associate metabolite spectral data to well eluates by retention time. UV/Vis absorbance spectra is shown in *purple*, total positive ion current is shown in *black*, and positive extracted ion is shown in *green* (*m/z* 509.7 $[M + H]^+$). *B*, percent positive cells for each injury signal was aligned to chromatograms to identify spectral regions with a bioactive component. *Green bars* indicate a hit for the respective marker. *C*, chemical structure of the isolated active component, narbomycin. *D*, biological response to metabolomic challenge increased from 24 to 48 h in wells containing narbomycin (*green 24*). All other wells identified in *black*, 1 to 30, were negative for biological signal.

staurosporine required 48 h to promote ATP release to the supernatant (Fig. 5*B*). In contrast to ATP secretion, no general trend from injury controls enhanced HMGB1 release to the supernatant (Fig. 5*C*). Rather, all compounds, except etoposide, reduced HMGB1 detection in the supernatant at 24 and 48 h compared to vehicle control (Fig. 5*C*). In the K562 model cell line, surface exposure of calreticulin was first detected at 24 h in staurosporine-challenged cells (Fig. 5*D*). By 48 h, all cell populations demonstrated a statistically significant increase of calreticulin surface expression compared to vehicle control (Fig. 5*D*).

Intracellular injury and extracellular immunogenic hallmarks were analyzed in conjunction by principal component analysis (Fig. 5*E*). Cells positive for cCAS3 and LC3 demonstrated ATP release and calreticulin externalization based on magnitude of negative correlation in PC2 by loadings analysis (Fig. S5*E*). On the other hand, markers p-MLKL, p-EIF2α, and p-HH3 were positively correlated with PC2 and failed to elevate ATP release as shown in Figure 5*B*. Notably, no compounds selectively enhanced release of HMGB1 to the supernatant (Fig. 5*B*) and it is the only readout with positive correlation to PC1 and PC2 (Fig. 5*E*). Based on this report, staurosporine-challenged cells are most likely to elicit cCAS3, eCRT, and ATP, which all presented strong negative correlations to PC2 in loadings analysis (Fig. 5*E*). Finally, nocodazole-treated cell populations were strongly linked to changes in p-EIF2α, p-MLKL, and p-HH3 revealed by the largest positive values in PC2 (Fig. 5*E*). Etoposide and thapsigargin by comparison were most likely to modulate HMGB1 while having little effect on other injury signals (Fig. 5*E*). It is notable that not all ICD signals shared positive signal correlation nor that any singular ICI guaranteed induction of ICD hallmarks.

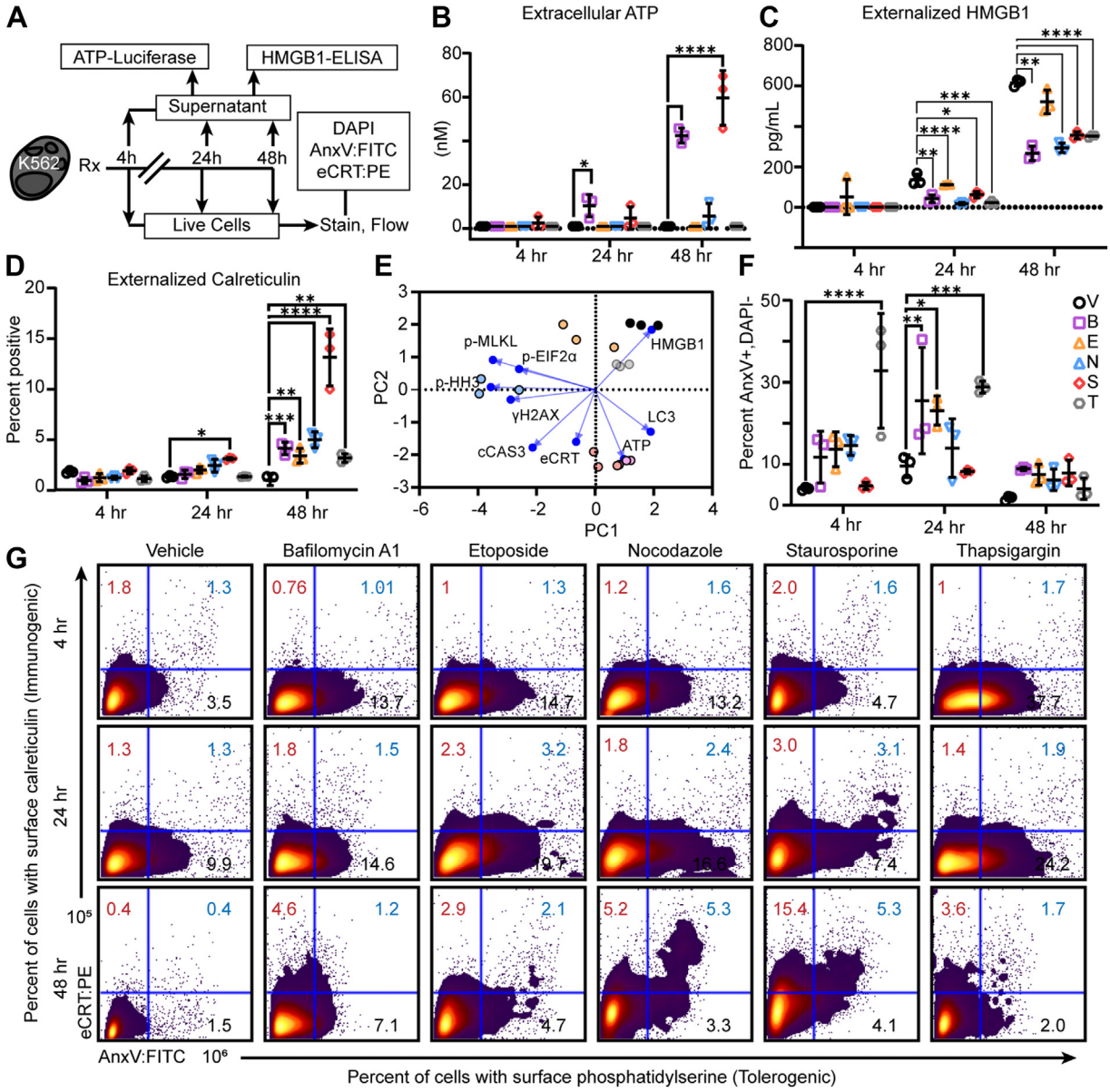

Figure 5. Secondary metabolites orient immunogenic hallmark intensity in leukemia model. *A*, K562 cells were challenged with 1 μM of compound or vehicle and sampled at 4, 24, and 48 h for detection of canonical immunogenic signals ATP, HMGB1, and externalized calreticulin (eCRT). *B*, extracellular ATP concentrations were determined from cell supernatant at each timepoint with Steady-Glo Luciferase Assay system. Scatter plots represent mean ± S.D. (n = 3, two-way ANOVA with Dunnett's multiple comparison test). *C*, extracellular HMGB1 concentrations were determined from cell supernatant at each timepoint with colorimetric HMGB1 ELISA. Scatter plots represent mean ± S.D. (n = 3, two-way ANOVA with Dunnett's multiple comparison test). *D*, externalized calreticulin was measured on live cells with fluorescent anti-calreticulin antibody at each timepoint and assessed as percent in gate of calreticulin-positive cells. Scatter plots show chemically induced fluorescent signal measured as percent in gate mean ± S.D. (n = 3, two-way ANOVA with Dunnett's multiple comparison test). *E*, nine continuous variables, six flow markers and three DAMPs, were standardized for parallel analysis with Monte Carlo simulations to calculate the eigenvalues of resulting principle components (PCs). PCs with eigenvalues that exceeded the 95th percentile of 1000 randomly seeded simulations were selected. Biplot revealed correlations of secondary metabolite influence on cell injury responses. *F*, viable 6-diamidino-2-phenylindole (DAPI) negative cells were evaluated for surface-exposed phosphatidylserine with annexin V:FITC (AnxV). Scatter plots show chemically induced fluorescent signal measured as percent in gate mean ± S.D (n = 3, two-way ANOVA with Dunnett's multiple comparison test). *G*, at each timepoint, live cells were stained for eCRT followed by staining with AnxV and the vital dye DAPI. Representative contour plots of biaxial gating for eCRT and AnxV. Percent-positive eCRT indicated in *red*, double-positive eCRT and AnxV in *blue*, and AnxV-positive in *black*. *p* *<0.05, **<0.01, ***<0.001, ****<0.0001. V, vehicle; B, bafilomycin A1; E, etoposide; N, nocodazole; S, staurosporine; T, thapsigargin; DAMP, damage associated molecular pattern.

In addition to measuring immunogenic eCRT, tolerogenic surface exposure of phosphatidylserine (sPS) in the outer leaflet of the plasma membrane was examined (53, 54). The sPS on live cells was measured with annexin V:FITC, and necrotic cells were labeled with the vital dye 6-diamidino-2-phenylindole (DAPI) (55, 56) (Figs. 5*F* and S14). Thapsigargin-treated cells displayed high levels of sPS at 4 and 24 h, as did etoposide, (Fig. 5, *F* and *G*) but remained DAPI negative (Fig. S14) with minimal calreticulin externalization (Fig. 5, *F* and *G*) and no cCAS3 induction (Fig. 2*D*), suggesting thapsigargin- and etoposide-induced sPS is not predictive of early apoptotic death nor necrosis under these conditions. Conversely, staurosporine failed to induce significant sPS and was the most positive control for eCRT after 48-h challenge

(Fig. 5, *F* and *G*) and supported immunogenicity of staurosporine-induced apoptosis (Fig. 5*E*). Bafilomycin A1 induced sPS at 24 h and limited calreticulin externalization through 48 h (Fig. 5, *D*, *F*, and *G*).

In total, the primary multiplexed assays applied in MAP and MAM with the cell injury module provided a workflow for the discovery of small molecule and natural product effectors of ICI. In turn, ICI signatures were used as a tool to advance active fractions to secondary DAMP assays and prioritize isolation of bioactive components. The compounds tested here both as pure compounds and spiked extracts interact with cellular processes that are conserved across cell types (*e.g.*, kinases, microtubules, SERCA, autophagy) and should ease application into other model systems without requiring specialized stimulation conditions or genetic modifications.

Discussion

It is unknown if current therapeutic regimens in the clinic optimally elicit antitumor responses in part because the relationship between cell injury, death, and immunogenicity is not completely defined. Moreover, successful ICD/injury therapies are largely confined to secondary metabolites (57). Analogs of established immunogenic compounds and scaffolds are evident in putative encoding biosynthetic gene clusters in genome sequenced organisms (58, 59); however, accessing these compounds is a labor and time-intensive process. The vast potential chemical reservoir confounds selection of producing organisms, which may also fail to synthesize the compound of interest under standard laboratory conditions. The fluorescent module presented here combined with MAP and MAM offer a high-throughput phenotypic screen for ICI signals. In turn, compounds for isolation can be prioritized by bioactivity in specific injury pathways, rather than overt cytotoxicity, as an indicator of antitumor potential.

A common feature of chemically induced immunogenicity is activation of damage response and cell stress signaling pathways including modulation of autophagy (8, 9, 11, 60), activation of the PERK arm of the UPR (10, 28, 60), DNA stress (12, 61), and certain death modalities (48, 62, 63) (Fig. 6). Inhibition of basal autophagy with the natural product bafilomycin A1 suspends degradation of cellular organelles by preventing acidification and fusion of autophagosomes and lysosome *via* v-ATPase blockade (Fig. 6) (31, 64). Inhibition in autophagy-competent cells is required for ICD but is not sufficient (65, 66). An additional necessary but insufficient ICD prerequisite is phosphorylation of translation initiation factor EIF2α at serine 51. This event stabilizes the inactive congener of EIF2B to prevent translation initiation (67–69). DNA damage is also a powerful immunogenic adjuvant in animal models (10). When multiple injury signals are present, the inhibition of autophagy, prolonged ER stress, or DNA damage can injure a cell such that apoptosis yields an immunogenic, rather than tolerogenic, response (6). Alternatively, necroptotic cell death is an ICI that releases DAMPs and promotes antitumor immunity in murine models (11). This form of programmed cell death requires phosphorylation of MLKL at serine 358 by the RIPK family of proteins (Fig. 6) (35, 36,

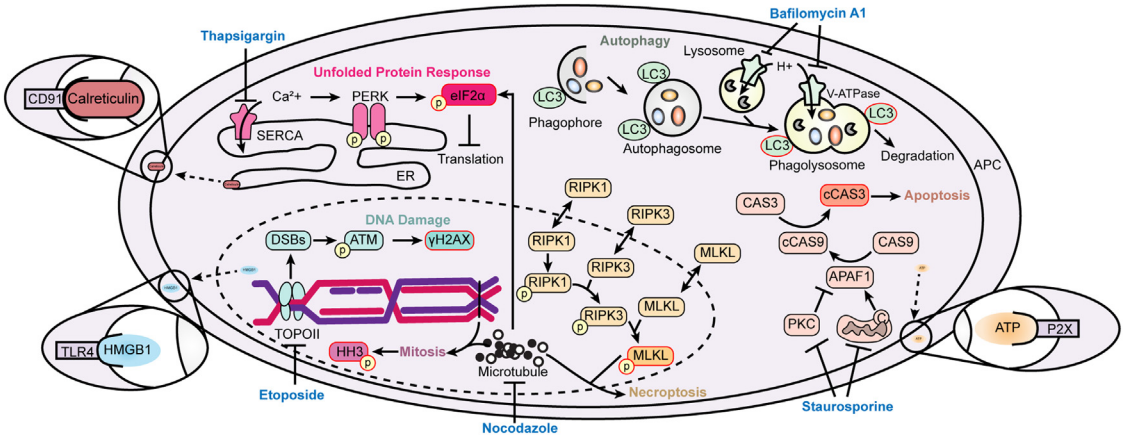

Figure 6. Secondary metabolite–directed cell injury model. Depiction of the six ICI mechanisms measured (color-coded pathways, *e.g.*, unfolded protein response) highlights the key readout for each signal (*pink highlighted boxes*, *e.g.*, p-EIF2α) and indicates a control compound characterized as a positive effector of the pathway (*blue text*, *e.g.*, thapsigargin). Thapsigargin inhibition of Ca-ATPase SERCA in the endoplasmic reticulum increases free calcium in the cytosol to trigger ER stress response pathways including the ER-resident transmembrane protein kinase, PERK, which phosphorylates eIF2α to inhibit translation until ER stress resolution. Bafilomycin A1 blocks autophagy by inhibiting V-ATPase on the lysosome and phagolysosome membranes thus hindering lumen acidification and subsequent activation of serine hydrolases therein. In turn, this prevents LC3 protein degradation on autophagic structures yielding increased levels of LC3. Staurosporine is canonically considered a pan-kinase inhibitor that occludes ATP-binding pockets. Staurosporine inhibition of PKC and mitochondria-localized enzymes result in disinhibition of APAF1, an apoptosome-related protein that facilitates conversion of CAS9 to its active form cCAS9 which then cleaves CAS3 to activate apoptotic hallmark cCAS3. Nocodazole binds beta-tubulin to prevent microtubule elongation. This prevents cellular division leading to enhanced levels of phosphorylated histone H3 protein. Additionally, microtubule inhibition can increase resident levels of the necroptotic execution protein p-MLKL. MLKL is phosphorylated following signal transduction *via* phosphorylation of RIPK1 and RIPK3 after exiting nuclear-cytosol cycling in response to stress. p-MLKL is trafficked to the cell membrane for oligomerization and insertion into the cell membrane leading to cell lysis. Etoposide forms a ternary complex with DNA and topoisomerase II to prevent religation of DNA yielding double strand breaks sensed by ATM. ATM then phosphorylates histone variant H2AX (γH2AX), which activates the DNA damage response to resolve double strand breaks. Literature evidence indicates inhibition and/or activation of these pathways can be proimmunogenic; however, the relative temporal relationship of these signals to enhance immunogenic cell death remains under investigated. To measure downstream cellular functions following ICI signaling mechanisms, three mechanisms of immunogenic cell death can be measured, namely calreticulin, HMGB1, and ATP. Each DAMP is shown interacting with respective surface receptors on an antigen presenting cell in *purple*. DAMP, damage associated molecular pattern; ICI, immunogenic cell injury.

70). Once phosphorylated, p-MLKL transverses the cell nucleus and cytosol along the microtubule network to form oligomers in the plasma membrane that promote cation influx to drive the final stages of necroptosis (36, 46). There is growing evidence that these injury signals, in addition to canonical DAMPs ATP, HMGB1, and eCRT, can indicate the potential for chemicals to generate an immunogenic response prior to advancing to animal and primary cell models.

By way of antibody validation, chemical induction, and barcoding, this work achieved detection of apoptotic, necroptotic, autophagic, mitotic, UPR, and DNA damage inducers in tandem for the first time in an unmodified cell system to generate chemically induced ICI profiles. These central death and damage response processes exemplified several pathways that contribute to immunogenic DAMP presentation. The secondary metabolite–mediated cell injury profiles presented here established benchmark control compounds for application of the ICI module to qualify and quantify bioactivity of unknown molecular agents in a discovery setting (Fig. 6). This discovery scheme identified new biological activity of the secondary metabolite narbomycin (Fig. 4) and will facilitate isolation of bioactive secondary metabolites that induce cellular injury relevant to downstream ICD.

Specific to the compound standards utilized here, early patterns corroborating ICI to ICD begin to emerge. For example, bafilomycin A1 and staurosporine enhanced LC3 and cCAS3 in varied time-dependent fashions, which confirmed natural products can modulate specific injury responses in sequence (Figs. 2 and 3). Staurosporine competes for binding pockets of ATP-dependent enzymes thus diminishing ATP hydrolysis (71, 72), while bafilomycin A1 prevents ATP turnover by rotational blockade of v-ATPase. Given these natural products inhibit two different cellular processes yet both elevate ATP secretion suggesting ATP hydrolysis blockade facilitated transference of ATP to the extracellular space, potentially as a consequence of elevated basal intracellular ATP levels. Cells can also engage the UPR to fine tune translation status as a reaction to endoplasmic reticulum stress. However, the inability of thapsigargin to elicit DAMPs ATP and HMG1 indicated p-EIF2α alone is not sufficient to induce a robust immunogenic response in this model (Fig. 5). This insufficiency is further supported by elevated detection of sPS in thapsigargin-treated cells as sPS can function as a tolerogenic signal (Fig. 5) (73, 74). How nocodazole inhibition of microtubules elicited the p-EIF2α phenotype is not clear (Fig. 6).

Since this assay unambiguously identifies hallmarks of ICI, it prioritizes secondary metabolites for isolation based on injury profiles to enrich for discovery and application of beneficially immunogenic natural products. Given the successful dereplication of narbomycin informed by bioactivity in an unknown extract and consistent signal induction by control compounds, the ICI module will be applied to additional unknown extracts in additional model systems and expand marker detection capacity to further define and elucidate the mechanistic relationships among types of ICI, more durable antitumor immunity, and adjuvanticity. One possible application of molecules inducing ICI is an *ex-vivo* treatment paradigm for prolonged immunological protection that obviates direct exposure to chemotherapies with debilitating side effects. For example, this injury module could be combined with cell identity modules (*e.g.*, leukemia stem cell populations) for characterization of cell injury cross-indexed by cell type and subtypes. In effect, ICI signatures of patient samples could infer and confirm optimal chemotherapies that target new cancer cell types and thus exposure of novel tumor antigens, as they arise during disease progression. Chemically induced ICI and subsequent ICD-activated cancer cells reintroduced to the patient could provide a continuous supply of personalized TAA vaccines that builds long term antitumor immunity. The addition of an antigen cross presentation assay would also help validate ICI candidates toward antitumor immunity studies in animals.

In summary, the workflow described herein simultaneously detected multiple markers of cell injury status in multiplexed samples of pure compounds or metabolomic fractions. This work described a new multiplexed panel entailing extensive optimization and development of two new antibody reagents for single cell detection and their optimization in an FCB workflow that balanced 10 fluorophores. This advanced on prior methods by transitioning FCB from traditional cytometry instruments to newer spectral flow cytometers (Cytek Aurora) and expanded this assay's detection capacity into three biological processes (autophagy, necroptosis, and UPR) in addition to apoptosis, DNA damage, and mitosis. This discovery system was built upon pioneering work in the ICD field (8, 10, 75, 76) to introduce the first cell-based assay that measured six ICI signals in tandem and explored time-dependent signal onset to chemical challenge. It also offered proof of principal for detection and discovery of new biologically active compounds in a chemically complex metabolomic sample. Indeed, the identification of narbomycin as a modulator of mammalian cell injury response from an extract of a previously uncharacterized microorganism illustrated discovery of new biological function in a known compound. The ICI module of the MAM platform will be applied to test injury-specific bioactivity in extracted actinobacteria metabolomes to inform natural product discovery, isolation of new ICI mediators, and fast-track interpretations of ICD that result in more durable antitumor immune responses. This will accelerate discovery of new compounds with immunogenic potential or elucidate novel immunogenic character of known compounds that may direct future pharmacological studies. Taken together, this work demonstrated a fluorescent high-throughput, high-fidelity assay that captured injury phenotypes in unmodified cells to focus discovery on novel chemical agents with immunogenic and therapeutic potential.

Experimental procedures

Processing: cell viability and fixation

Following treatment of cells with compounds, vehicle or metabolomic fractions, 200 μl of cells (1 million cells/ml),

were stained with 20 μl of A × 700 (Thermo A20010, stock concentration 20 μg/ml) to a final concentration of 0.04 μg/ml 37 °C for 20 min and protected from light. Cells were then transferred to 96 well V-bottom polypropylene plate with 20 μl of 20% paraformaldehyde (PFA) (Alfa Aesar 47340) for a final PFA concentration of 1.6% for 10 min at room temperature, protected from light. Plate was centrifuged at 800 g for 5 min, supernatant decanted by plate inversion, and dabbed dry on a Kimwipe (Kimtech 34155). The plate was then vortexed, and cells were permeabilized with 200 μl ice-cold MeOH for at least 20 minutes at −20 °C. After permeation and prior to FCB, cells were centrifuged at 800*g* for 5 min, decanted by inversion, vortexed, and resuspended in 200 μl PBS (Gibco 10010-023).

Processing: fluorescent cell barcoding

Eight 1:1.7 serial dilutions of Pacific Blue (Thermo P10163) were prepared in DMSO at concentrations ranging from 10 μg/ml to 0.24 μg/ml. Six 1:1.7 serial dilution stock concentrations of Pacific Orange (Thermo P30253) were prepared in DMSO at concentrations ranging from 40 μg/ml to 2.82 μg/ml. A × 750 (Thermo A20011) 500 μg/ml stock solution in DMSO was prepared at 5 μg/ml. All three dyes were combined on a single V-bottom polypropylene master plate as follows: 50 μl of Pacific Blue were added to plate rows with the highest concentration in row A and the lowest concentration in row H; 50 μl of Pacific Orange were added to columns with the highest concentration in column 1 and lowest concentration in column 6; 50 μl of A × 750 were added to all wells. Master plates were then aliquoted in 15 μl volumes to 96-well V-bottom propylene plates and stored at −20 °C. An aliquot of 185 μl of fixed/permeabilized cells in PBS were added to 15 μl of barcode dyes and stained for 15 min at room temperature, protected from light. Barcoding reactions were quenched with 70 μl 2% bovine serum albumin (BSA) in PBS, centrifuged at 800 g for 5 min, decanted by inversion, vortexed, washed with 200 μl 2% BSA in PBS, centrifuged at 800 g for 5 min, decanted by inversion, and vortexed. Wells in column 1 were then resuspended in 200 μl of 2% BSA in PBS then transferred to column 2 and repeated to column 6. All rows in column 6 were then pooled into 1 flow cytometry tube.

Processing: flow cytometry data acquisition

Flow cytometry data was acquired on four laser (405 nM, 488 nM, 561 nM, and 640 nM) Cytek Biosciences Aurora spectral flow cytometer following spectral unmixing with single color reference controls. Data was uploaded and stored in Cytobank for gating, compensation, and analysis of unmixed cytometry data files (FCS file format). Quality control (QC) gating consisted of QC1: FSC-A versus SSC-A for cell bodies, QC2: FSC-A versus FSC-W for singlets, and FSC-A versus A × 700 for viable cells. Unmixed FCB samples were QC gated with addition of QC4: FSC-A versus A × 750 for barcode uptake control, compensated, then debarcoded with DebarcodeR to produce one FCS file per well and uploaded to Cytobank for storage and further analysis.

Multiplexing: validation panel

K562 cells were challenged with a final concentration of 10 μM of thapsigargin in hanks balanced salt solution (Corning 21-021-CV) or 10 μM etoposide or nocodazole in cRPMI for 24 h or DMSO vehicle control. Cells were fixed in a final concentration of 1.6% PFA, permeabilized with ice-cold MeOH, and stained with *N*-hydroxy succinimide (NHS)-functionalized Pacific Blue, Pacific Orange, or A × 750 dyes (1 color/condition) pooled (3 conditions) into a single flow cytometry tube and stained with antibody cocktail of γH2AX:Percp-Cy5.5 (BD 564718, 2.5:100) and p-MLKL (CST 91689S 5:100) or p-EIF2α (CST 3597L 5:100) in 100 μl of 2% BSA in PBS for 30 minutes in the dark. Staining was quenched with 1 ml of 2% BSA in PBS, centrifuged at 800 g for 5 min, and decanted by inversion. Flow cytometry tube was vortexed and washed with 1 ml of 2% BSA in PBS, centrifuged at 800 g for 5 min, decanted by inversion, vortexed and resuspended in 200 μl 2% BSA in PBS. Rabbit antibodies p-MLKL and p-EIF2α were detected with Gt α Rb:488 fluorescent secondary antibody at 1:5000 by staining for 30 min at room temperature in the dark in a final volume of 400 μl. Cells were washed with 2% BSA in PBS as described above prior to analysis. This process was repeated following antibody conjugation with the exception of Gt α Rb A × 488 fluorescent secondary antibody and addition of p-MLKL:568 or p-EIF2α:647 (5:100).

Multiplexing: antibody conjugation

Antibody p-MLKL was conjugated to A × 568 with Thermofisher antibody labeling kit A20184 adapted from manufacturer's instruction. Antibody p-EIF2α was conjugated to A × 647with Thermofisher antibody labeling kit A20186 adapted from manufacturer's instructions. In brief, antibody storage solution was removed by 10 kDa M.W. concentrator tubes (Pierce 88513) with 100 mM sodium bicarbonate. Tubes were spun at 11,000*g* for 3 min, flow through discarded, and 100 μl of 100 mM sodium bicarbonate added to concentrator tube. This process was repeated thrice. Pure antibodies were harvested and incubated with specified antibody labeling kit in 100 μl volume of 100 mM sodium bicarbonate for 1 h in the dark with mixing. Excess dye was removed by purification resin provided by the manufacturer. Antibodies were stored in antibody storage solution consistent with manufacturer's recommendation. Fluorescent intensity of conjugated antibody was evaluated by SDS-PAGE fluorescence gel in reduced and nonreduced condition. Antibodies were prepared in Tris/SDS/Glycine running buffer and Laemmli sample buffer ± BME incubated at room temperature for 5 min and heated to 95 °C for 5 min then centrifuged. Samples were loaded onto a 4 to 20% Tris/Glycine gel and electrophoresed for 60 min at 175 V. Gels were imaged with a Biorad Chemidoc MP Imaging System.

Multiplexing: injury panel

Cells were stained with fluorescent antibodies LC3:A × 488 (CST 13082, 1:100), γH2AX:Percp-Cy5.5 (BD 564718, 2.5:100),

cCAS3:PE (10:100), p-MLKL:A × 568 (CST 91689S 5:100), p-HH3:Pe-Cy7 (Biolegend 6410, 1:1000), p-EIF2α:A × 647 (CST 3597L 5:100) in 100 μl of 2% BSA in PBS for 30 min in the dark. Staining was quenched with 2% BSA in PBS, sample centrifuged at 800*g* for 5 min, decanted by inversion, repeated once, and resuspended in 200 μl 2% BSA in PBS prior to analysis.

Multiplexing: live cell panel

Cells were treated with 1 μM of control compounds for 4, 24, or 48 h. At each timepoint, cells were viability stained with A × 700, then stained with Calreticulin:PE (CST 19780, 1:50) for 30 min in the dark on ice. Cells were washed with 2% BSA in PBS then stained with annexin V:FITC and a final concentration of 1 μM DAPI in annexin-binding buffer on ice. annexin V:FITC and DAPI were not washed prior to live cell data acquisition consistent with manufacturer's instructions (CST 6592). DAPI was used to replace PI.

Profiling: cell culture

K562, Jurkat, and MV-4-11 cell lines were a generous gift from the Ferrell lab and confirmed to be *mycoplasma* negative. K562 and Jurkat were cultured in complete RPMI (cRPMI) consisting of RPMI 1640 (Gibco 22400-089) supplemented to a final concentration of 10% heat inactivated fetal bovine serum (Gibco 16140-071), 1 mM sodium pyruvate (Gibco 11360-070), and 1% penicillin/streptomycin cocktail (Gibco 15140-122). MV-4-11 were cultured in IMDM (Gibco 12440-053), supplemented to a final concentration of 10% fetal bovine serum. Cells were incubated in a water jacketed 5% CO_2 incubator at 37 °C. Cells were maintained at densities between 100 thousand and 1 million cells per ml of culture media, fed every other day, and passaged every 4 days.

Profiling: MAP for signal specificity

Control compounds bafilomycin A1, etoposide, nocodazole, staurosporine, and thapsigargin were acquired from Selleckchem as noted in supporting information. Compound stock solutions were prepared at 200 × and diluted $\log_{10}$ across four wells for final concentration ranging from 10 μM to 10 nM. One microliters of 200 × of each compound concentrations were added to respective wells and resuspended in 200 μl of cell containing media. At each timepoint, cells were fixed, permeabilized, fluorescently barcoded, and stained as described above. K562 CML, MV-4-11 B-myelomonocytic leukemia, and Jurkat T lymphoblastic leukemia cell models were treated with $\log_{10}$ series dilution from 10 μM to 10 nM and incubated for 4, 24, or 48 h (Figs. 2*A* and S4). At each timepoint, cells were stained for viability with A × 700, fixed, and permeabilized as described above. Cells were FCB by well coordinates with an array of eight NHS-PB concentrations by six NHS-PO concentrations as well as one dye uptake control NHS-Ax750 concentration, then pooled for homogenous staining with a fluorescent antibody cocktail consisting of six unique target:fluorophore combinations including: LC3:488, γH2AX:PCPC5, cCAS3:PE, p-MLKL:568, p-HH3:PEC7, and p-EIF2α:647, to yield a 10 color fluorescent injury panel (Fig. 2*A* and Table S2). Barcoding and pooling reduce sample-to-sample staining variability and processing by incubating all samples with the same fluorescent antibody cocktail over equivalent time intervals and temperatures while also saving on costly antibody reagents and decreasing instrument use time. Secondary metabolite–induced injury phenotype data were acquired on single cells on a Cytek Aurora spectral flow cytometer and uploaded to Cytobank for storage and processing (77). Collected cellular events were quality control gated for viable-singlets and control NHS-Ax750 barcode dye uptake (Fig. 2*B*). Barcoded cells were digitally reassigned to origin plate wells with the DebarcodeR (42) algorithm (Fig. 2*B*). Cells were processed and stained for analysis as described above (Fig. 2*D*) with the exception of dose variability.

Profiling: crude microbial extract preparation

Laboratory isolate strain KPBlue13 (99% 16S sequence identity *S. pratensis*) and KPBlue17 (99% 16S sequence identity *Streptomyces exfoliates*) were isolated from Blue Spring Cave (in Sparta, TN) and was maintained on ISP2 agar (yeast extract 4 g/l, malt extract 10 g/l, glucose 4 g/l, and agar 17.5 g/l, pH 7.2). Loops of mycelia were used to inoculate 25 ml seed cultures in ISP2 medium (yeast extract 4 g/l, malt extract 10 g/l, and glucose 4 g/l, pH 7.2) incubating for 2 days at 30 °C. Seed cultures were then transferred to 250-ml Erlenmeyer flasks containing 25 ml of ISP2 and grown for 7 days at 30 °C with shaking. Aqueous fermentation broth was extracted by shaking with Diaion HP20 synthetic absorbent resin (Alfa Aesar) (125 ml of HP20 bead/H_2O slurry per 500 ml of aqueous broth) for 2 h. Fermentation broth was then centrifuged (3700*g*, 30 min) and the supernatant was decanted. Metabolites were eluted from absorbent resin and cells were eluted with methanol (250 ml of methanol/125 ml of HP20 bead/H2O slurry) by shaking for 1.5 h, followed by centrifugation (3700*g*, 30 min) and decanting the methanol extract. Further extraction was performed with acetone (250 ml of acetone/125 ml of HP20 bead/H2O slurry) by shaking for 1.5 h, followed by centrifugation (3700*g*, 30 min) and decanting the acetone extract. Methanol and acetone extracts were combined and lyophilized with Series 3 HT 6 Genevac with manufacturer's HPLC-Lyo method and stored at −20 °C.

Profiling: generation of metabolomic arrays

Mass spectrometry was performed by using a TSQ Triple Quantum mass spectrometer equipped with an electrospray ionization source and Surveyor PDA Plus detector. For positive ion mode, the following settings were used: capillary temperature 270 °C; spray voltage 4.2 kV; spray current 30 mA; capillary voltage 35 V; tube lens 119 V; and skimmer offset 15 V. For negative ion mode, capillary temperature 270 °C; spray voltage 30 kV; spray current 20 mA; capillary voltage 35 V; tube lens 119 V; and skimmer offset 15 V.

Fractionated plates were prepared by injecting 20 μl of purified compounds in HPLC-grade methanol or concentrated extract *via* a Thermo PAL auto injector onto a Phenomenex Luna 5 μm C18(2) reverse-phase C_{18} HPLC column. The sample was fractionated using a gradient of 100% buffer A (95% H_2O, 5% acetonitrile) to 100% buffer B (5% acetonitrile, 95% H_2O) over 30 min at a flow rate of 1 ml/min and split in a 3:1 ratio with three parts going to the photodiode array detector and fraction collector and one part going to the MS. Fractions were collected in 1-min intervals in a 96 deep well plate. A volume of 150 μl of eluent from each well was transferred to four replica 96-well plates and dried in vacuo using a Series 3 HT-6 Genevac system with manufacturer's HPLC-Lyo protocol.

Profiling: MAM with internal standards

Dimethyl sulfoxide stock solutions of nocodazole (1 μl, 20 mM), staurosporine (1 μl, 20 mM), and bafilomycin A1 (4 μl, 5 mM) were added to 44 μl of crude extract at 100 mg/ml in HPLC-grade methanol and fractionated and lyophilized as described above. Wells were resuspended in 200 μl of media containing cells, incubated, and processed for flow cytometry as described above.

Assay: luciferase ATP

Extracellular ATP was evaluated with Cell Titer-Glo 2.0 Luciferase Assay System (Promega G9241) adapted from manufacturer's instructions. Briefly, at each timepoint, cell supernatant from treated cells was mixed 1:1 with Cell Titer-Glo reagent, in an opaque, white bottom plate, incubated at room temperature for 10 min, then signal for total luminescence was acquired with a Biotek Synergy H4 Hybrid reader. Standard curves were generated for calculation of ATP concentrations. Samples below the limit of detection were assigned a unit value of 1. K562 were challenged cells with 1 μM of injury controls and incubated for 4, 24, and 48 h (Fig. 4*A*). At each time point, cell supernatants were harvested and split to evaluate ATP release with a recombinant luciferase (Promega, E2510) or HMGB1 ejection by ELISA (NovusBio, NBP2-62766) in accordance with manufacturers protocols (Fig. 4*A*).

Assay: HMGB1 ELISA

Extracellular HMGB1 was evaluated with human HMGB1/HMG-1 colorimetric ELISA kit (Novus #NBP2-62766) adapted from manufacturer's instructions with the exception that harvested cell supernatants at each timepoint were diluted 1:9 in PBS prior to plating. Absorbance data was acquired a Biotek Synergy H4 Hybrid reader. Standard curves were generated for back calculation of HMGB1 concentrations. Samples below the limit of detection were assigned a unit value of 1.

Data: statistical analysis and figure generation

Data was input to Graph Pad Prism (9.2.0) and analyzed with one-way or two-way ANOVA according to figure legends. All data is reported as mean ± SD of at least three biological replicates. Prism, Adobe Illustrator 2021, and Microsoft Excel 2016 were used for figure generation. Principal component analysis was performed on nine continuous variables that were standardized for parallel analysis with Monte Carlo simulations to calculate the eigenvalues of resulting principle components (PCs). PCs with eigenvalues that exceeded the 95th percentile of 1000 randomly seeded simulations were selected for PC axes.

Data availability

Correspondence and requests for materials should be addressed to the corresponding author (brian.bachmann@vanderbilt.edu).

Supporting information—This article contains supporting information, supporting Figures 1–14 and supporting Tables 1 and 2.

Acknowledgments—The authors are grateful to Kelsey Pilewski and Manuel Castro for valuable input during manuscript preparation. Special thanks to David Flaherty and Brittany Matlock of the VUMC Flow Cytometry Shared Resource for instrument training and scheduling. Flow Cytometry experiments were performed in the VUMC Flow Cytometry Shared Resource. The authors thank the National Institutes of Health for research R01 GM092218, R01 CA226833, and training support T32 GM07628. The VUMC Flow Cytometry Shared Resource is supported by the Vanderbilt Ingram Cancer Center (P30 CA68485) and the Vanderbilt Digestive Disease Research Center (DK058404).

Author contributions—J. M. I. and B. O. B. conceptualization; J. M. I. and B. O. B. funding acquisition; J. A. B. formal analysis; J. A. B. methodology; J. A. B., K. E. P., and Z. Z. investigation; J. A. B. and M. J. H. resources, J. A. B. and S. M. L. software; J. A. B., K. E. P., Z. Z., M. J. H., S. M. L., J. M. I., and B. O. B. visualization; J. A. B., K. E. P., Z. Z., M. J. H., S. M. L., J. M. I., and B. O. B. writing–review and editing.

Funding and additional information—The content is solely the responsibility of the authors and does not necessarily represent the official views of the National Institutes of Health.

Conflict of interest—The authors declare no conflict of interest.

Abbreviations—The abbreviations used are: DAMP, damage associated molecular pattern; DAPI, 6-diamidino-2-phenylindole; FCB, fluorescent cell barcoding; ICD, immunogenic cell death; ICI, immunogenic cell injury; MAM, multiplexed activity metabolomics; MAP, multiplexed activity profiling; PC, principle component; QC, quality control; sPS, phosphatidylserine; v-ATPase, vacuolar H+-ATPase.

References

1. Newman, D. J., and Cragg, G. M. (2016) Natural products as sources of new drugs from 1981 to 2014. *J. Nat. Prod.* **79**, 629–661
2. Miura, M. (2015) Therapeutic drug monitoring of imatinib, nilotinib, and dasatinib for patients with chronic myeloid leukemia. *Biol. Pharm. Bull.* **38**, 645–654
3. Lown, J. W. (1993) Discovery and development of anthracycline antitumour antibiotics. *Chem. Soc. Rev.* **22**, 165

4. Horwitz, S. B. (1994) Taxol (paclitaxel): mechanisms of action. *Ann. Oncol.* **5**, S3–S6
5. World Health Organization Model List of Essential Medicines – 22nd List, 2021. Geneva: World Health Organization; 2021 (WHO/MHP/HPS/EML/2021.02). Licence: CC BY-NC-SA 3.0 IGO
6. Casares, N., Pequignot, M. O., Tesniere, A., Ghiringhelli, F. O., Roux, S. P., Chaput, N., *et al.* (2005) Caspase-dependent immunogenicity of doxorubicin-induced tumor cell death. *J. Exp. Med.* **202**, 1691–1701
7. Minute, L., Teijeira, A., Sanchez-Paulete, A. R., Ochoa, M. C., Alvarez, M., Otano, I., *et al.* (2020) Cellular cytotoxicity is a form of immunogenic cell death. *J. Immunother. Cancer* **8**, e000325
8. Martins, I., Michaud, M., Sukkurwala, A. Q., Adjemian, S., Ma, Y., Shen, S., *et al.* (2012) Premortem autophagy determines the immunogenicity of chemotherapy-induced cancer cell death. *Autophagy* **8**, 413–415
9. Michaud, M., Martins, I., Sukkurwala, A. Q., Adjemian, S., Ma, Y., Pellegatti, P., *et al.* (2011) Autophagy-dependent anticancer immune responses induced by chemotherapeutic agents in mice. *Science* **334**, 1573–1577
10. Bezu, L., Sauvat, A., Humeau, J., Gomes-Da-Silva, L. C., Iribarren, K., Forveille, S., *et al.* (2018) eIF2α phosphorylation is pathognomonic for immunogenic cell death. *Cell Death Differ.* **25**, 1375–1393
11. Aaes, L., Tania, Kaczmarek, A., Delvaeye, T., Craene, D., Bram, Koker, D., Stefaan, Heyndrickx, L., *et al.* (2016) Vaccination with necroptotic cancer cells induces efficient anti-tumor immunity. *Cell Rep.* **15**, 274–287
12. Sriram, G., Milling, L. E., Chen, J.-K., Kong, Y. W., Joughin, B. A., Abraham, W., *et al.* (2021) The injury response to DNA damage in live tumor cells promotes antitumor immunity. *Sci. Signal.* **14**, eabc4764
13. Aurelius, J., Möllgård, L., Kiffin, R., Ewald Sander, F., Nilsson, S., Thorén, F. B., *et al.* (2019) Anthracycline-based consolidation may determine outcome of post-consolidation immunotherapy in AML. *Leuk. Lymphoma* **60**, 2771–2778
14. Lecciso, M., Ocadlikova, D., Sangaletti, S., Trabanelli, S., De Marchi, E., Orioli, E., *et al.* (2017) ATP release from chemotherapy-treated dying leukemia cells elicits an immune suppressive effect by increasing regulatory T cells and tolerogenic dendritic cells. *Front. Immunol.* **8**, 1918
15. Park, S. J., Ye, W., Xiao, R., Silvin, C., Padget, M., Hodge, J. W., *et al.* (2019) Cisplatin and oxaliplatin induce similar immunogenic changes in preclinical models of head and neck cancer. *Oral Oncol.* **95**, 127–135
16. Bains, S. J., Abrahamsson, H., Flatmark, K., Dueland, S., Hole, K. H., Seierstad, T., *et al.* (2020) Immunogenic cell death by neoadjuvant oxaliplatin and radiation protects against metastatic failure in high-risk rectal cancer. *Cancer Immunol. Immunother.* **69**, 355–364
17. Galluzzi, L., Vitale, I., Warren, S., Adjemian, S., Agostinis, P., Martinez, A. B., *et al.* (2020) Consensus guidelines for the definition, detection and interpretation of immunogenic cell death. *J. Immunother. Cancer* **8**, e000337
18. Yatim, N., Jusforgues-Saklani, H., Orozco, S., Schulz, O., Barreira Da Silva, R., Reis E Sousa, C., *et al.* (2015) RIPK1 and NF- B signaling in dying cells determines cross-priming of CD8+ T cells. *Science* **350**, 328–334
19. Efimova, I., Catanzaro, E., Van Der Meeren, L., Turubanova, V. D., Hammad, H., Mishchenko, T. A., *et al.* (2020) Vaccination with early ferroptotic cancer cells induces efficient antitumor immunity. *J. Immunother. Cancer* **8**, e001369
20. Liu, P., Zhao, L., Loos, F., Iribarren, K., Lachkar, S., Zhou, H., *et al.* (2017) Identification of pharmacological agents that induce HMGB1 release. *Sci. Rep.* **7**, 14915
21. Sansone, C., Bruno, A., Piscitelli, C., Baci, D., Fontana, A., Brunet, C., *et al.* (2021) Natural compounds of marine origin as inducers of immunogenic cell death (ICD): potential role for cancer interception and therapy. *Cells* **10**, 231
22. Xie, B., He, X., Guo, G., Zhang, X., Li, J., Liu, J., *et al.* (2020) High-throughput screening identified mitoxantrone to induce death of hepatocellular carcinoma cells with autophagy involvement. *Biochem. Biophys. Res. Commun.* **521**, 232–237
23. Kuo, L. J., and Yang, L. X. (2008) γ-H2AX-a novel biomarker for DNA double-strand breaks. *In Vivo* **22**, 305–309
24. Burma, S., Chen, B. P., Murphy, M., Kurimasa, A., and Chen, D. J. (2001) ATM phosphorylates histone H2AX in response to DNA double-strand breaks. *J. Biol. Chem.* **276**, 42462–42467
25. Belmokhtar, C. A., Hillion, J., and Ségal-Bendirdjian, E. (2001) Staurosporine induces apoptosis through both caspase-dependent and caspase-independent mechanisms. *Oncogene* **20**, 3354–3362
26. Malsy, M., Bitzinger, D., Graf, B., and Bundscherer, A. (2019) Staurosporine induces apoptosis in pancreatic carcinoma cells PaTu 8988t and Panc-1 *via* the intrinsic signaling pathway. *Eur. J. Med. Res.* **24**, 5
27. Earl, D. C., Ferrell, P. B., Leelatian, N., Froese, J. T., Reisman, B. J., Irish, J. M., *et al.* (2018) Discovery of human cell selective effector molecules using single cell multiplexed activity metabolomics. *Nat. Commun.* **9**, 39
28. Bezu, L., Sauvat, A., Humeau, J., Leduc, M., Kepp, O., and Kroemer, G. (2018) eIF2α phosphorylation: a hallmark of immunogenic cell death. *OncoImmunology* **7**, e1431089
29. Mauvezin, C., and Neufeld, T. P. (2015) Bafilomycin A1 disrupts autophagic flux by inhibiting both V-ATPase-dependent acidification and Ca-P60A/SERCA-dependent autophagosome-lysosome fusion. *Autophagy* **11**, 1437–1438
30. Yamamoto, A., Tagawa, Y., Yoshimori, T., Moriyama, Y., Masaki, R., and Tashiro, Y. (1998) Bafilomycin A1 prevents maturation of autophagic vacuoles by inhibiting fusion between autophagosomes and lysosomes in rat hepatoma cell line, H-4-II-E cells. *Cell Struct. Funct.* **23**, 33–42
31. Wang, R., Wang, J., Hassan, A., Lee, C.-H., Xie, X.-S., and Li, X. (2021) Molecular basis of V-ATPase inhibition by bafilomycin A1. *Nat. Commun.* **12**, 1782
32. Sehgal, P., Szalai, P., Olesen, C., Praetorius, H. A., Nissen, P., Christensen, S. B., *et al.* (2017) Inhibition of the sarco/endoplasmic reticulum (ER) Ca2+-ATPase by thapsigargin analogs induces cell death *via* ER Ca2+ depletion and the unfolded protein response. *J. Biol. Chem.* **292**, 19656–19673
33. Xu, C., Ma, H., Inesi, G., Al-Shawi, M. K., and Toyoshima, C. (2004) Specific structural requirements for the inhibitory effect of thapsigargin on the Ca2+ ATPase SERCA. *J. Biol. Chem.* **279**, 17973–17979
34. Lytton, J., Westlin, M., and Hanley, M. R. (1991) Thapsigargin inhibits the sarcoplasmic or endoplasmic reticulum Ca-ATPase family of calcium pumps. *J. Biol. Chem.* **266**, 17067–17071
35. Rodriguez, D. A., Weinlich, R., Brown, S., Guy, C., Fitzgerald, P., Dillon, C. P., *et al.* (2016) Characterization of RIPK3-mediated phosphorylation of the activation loop of MLKL during necroptosis. *Cell Death Differ.* **23**, 76–88
36. Weber, K., Roelandt, R., Bruggeman, I., Estornes, Y., and Vandenabeele, P. (2018) Nuclear RIPK3 and MLKL contribute to cytosolic necrosome formation and necroptosis. *Commun. Biol.* **1**, 6
37. Sarhan, J., Liu, B. C., Muendlein, H. I., Weindel, C. G., Smirnova, I., Tang, A. Y., *et al.* (2019) Constitutive interferon signaling maintains critical threshold of MLKL expression to license necroptosis. *Cell Death Differ.* **26**, 332–347
38. Vasquez, R. J., Howell, B., Yvon, A. M., Wadsworth, P., and Cassimeris, L. (1997) Nanomolar concentrations of nocodazole alter microtubule dynamic instability *in vivo* and *in vitro*. *Mol. Biol. Cell* **8**, 973–985
39. Frank, T., Tuppi, M., Hugle, M., Dötsch, V., Van Wijk, S. J. L., and Fulda, S. (2019) Cell cycle arrest in mitosis promotes interferon-induced necroptosis. *Cell Death Differ.* **26**, 2046–2060
40. Krutzik, P. O., Clutter, M. R., Trejo, A., and Nolan, G. P. (2011) Fluorescent cell barcoding for multiplex flow cytometry. *Curr. Protoc. Cytom.* **55**, 6–31
41. Boyce, J. H., Reisman, B. J., Bachmann, B. O., and Porco, J. A., Jr. (2021) Synthesis and multiplexed activity profiling of synthetic acylphloroglucinol scaffolds. *Angew. Chem. Int. Ed. Engl.* **60**, 1263–1272
42. Reisman, B. J., Barone, S. M., Bachmann, B. O., and Irish, J. M. (2021) DebarcodeR increases fluorescent cell barcoding capacity and accuracy. *Cytometry Part A* **99**, 946–953
43. Krutzik, P. O., and Nolan, G. P. (2006) Fluorescent cell barcoding in flow cytometry allows high-throughput drug screening and signaling profiling. *Nat. Met.* **3**, 361–368
44. Hori, T., Maezawa, I., Nagahama, I., and Suzuki, N. (1971) Isolation and structure of narbonolide, narbomycin aglycone, from Streptomyces venezuelae and its biological transformation into picromycin *via* narbomycin. *J. Chem. Soc. D: Chem. Commun.*, 304–305

45. Amodio, G., Moltedo, O., Fasano, D., Zerillo, L., Oliveti, M., Di Pietro, P., *et al.* (2019) PERK-mediated unfolded protein response activation and oxidative stress in PARK20 fibroblasts. *Front. Neurosci.* **13**, 673
46. Samson, A. L., Zhang, Y., Geoghegan, N. D., Gavin, X. J., Davies, K. A., Mlodzianoski, M. J., *et al.* (2020) MLKL trafficking and accumulation at the plasma membrane control the kinetics and threshold for necroptosis. *Nat. Commun.* **11**, 3151
47. Perez, E. A. (2009) Microtubule inhibitors: differentiating tubulin-inhibiting agents based on mechanisms of action, clinical activity, and resistance. *Mol. Cancer Ther.* **8**, 2086–2095
48. Sauler, M., Bazan, I. S., and Lee, P. J. (2019) Cell death in the lung: the apoptosis–necroptosis Axis. *Annu. Rev. Physiol.* **81**, 375–402
49. Moriwaki, K., and Chan, F. K.-M. (2017) The inflammatory signal adaptor RIPK3: functions beyond necroptosis. In **, 328**. *Int. Rev. Cell. Mol. Biol.*, Elsevier, Cambridge, MA: 253–275
50. Toriyama, K., Takano, N., Kokuba, H., Kazama, H., Moriya, S., Hiramoto, M., *et al.* (2021) Azithromycin enhances the cytotoxicity of DNA-damaging drugs *via* lysosomal membrane permeabilization in lung cancer cells. *Cancer Sci.* **112**, 3324–3337
51. Hirasawa, K., Moriya, S., Miyahara, K., Kazama, H., Hirota, A., Takemura, J., *et al.* (2016) Macrolide antibiotics exhibit cytotoxic effect under amino acid-depleted culture condition by blocking autophagy flux in head and neck squamous cell carcinoma cell lines. *PLoS One* **11**, e0164529
52. Mukai, S., Moriya, S., Hiramoto, M., Kazama, H., Kokuba, H., Che, X.-F., *et al.* (2016) Macrolides sensitize EGFR-TKI-induced non-apoptotic cell death *via* blocking autophagy flux in pancreatic cancer cell lines. *Int. J. Oncol.* **48**, 45–54
53. Naeini, M. B., Bianconi, V., Pirro, M., and Sahebkar, A. (2020) The role of phosphatidylserine recognition receptors in multiple biological functions. *Cell Mol. Biol. Lett.* **25**, 23
54. Shlomovitz, I., Speir, M., and Gerlic, M. (2019) Flipping the dogma – phosphatidylserine in non-apoptotic cell death. *Cell Commun. Signal.* **17**, 139
55. Wallberg, F., Tenev, T., and Meier, P. (2016) Analysis of apoptosis and necroptosis by fluorescence-activated cell sorting. *Cold Spring Harb. Protoc.* **2016**. pdb prot087387
56. Martins, I., Tesniere, A., Kepp, O., Michaud, M., Schlemmer, F., Senovilla, L., *et al.* (2009) Chemotherapy induces ATP release from tumor cells. *Cell Cycle* **8**, 3723–3728
57. Menger, L., Vacchelli, E., Adjemian, S., Martins, I., Ma, Y., Shen, S., *et al.* (2012) Cardiac glycosides exert anticancer effects by inducing immunogenic cell death. *Sci. Transl. Med.* **4**, 143ra99
58. Bachmann, B. O., Lanen, Van, S. G, and Baltz, R. H. (2014) Microbial genome mining for accelerated natural products discovery: is a renaissance in the making? *J. Ind. Microbiol. Biotechnol.* **41**, 175–184
59. Kenshole, E., Herisse, M., Michael, M., and Pidot, S. J. (2021) Natural product discovery through microbial genome mining. *Curr. Opin. Chem. Biol.* **60**, 47–54
60. Popat, A., Patel, A., and Warnes, G. (2019) A flow cytometric study of ER stress and autophagy. *Cytometry A* **95**, 672–682
61. Viswesh, V., Gates, K., and Sun, D. (2010) Characterization of DNA damage induced by a natural product antitumor antibiotic leinamycin in human cancer cells. *Chem. Res. Toxicol.* **23**, 99–107
62. Tang, R., Xu, J., Zhang, B., Liu, J., Liang, C., Hua, J., *et al.* (2020) Ferroptosis, necroptosis, and pyroptosis in anticancer immunity. *J. Hematol. Oncol.* **13**, 110
63. Han, W., Sun, J., Feng, L., Wang, K., Li, D., Pan, Q., *et al.* (2011) Autophagy inhibition enhances daunorubicin-induced apoptosis in K562 cells. *PLoS One* **6**, e28491
64. Mauvezin, C., Nagy, P., Juhász, G., and Neufeld, T. P. (2015) Autophagosome–lysosome fusion is independent of V-ATPase-mediated acidification. *Nat. Commun.* **6**, 7007
65. Wang, Y., Xie, W., Humeau, J., Chen, G., Liu, P., Pol, J., *et al.* (2020) Autophagy induction by thiostrepton improves the efficacy of immunogenic chemotherapy. *J. Immunother. Cancer* **8**, e000462
66. Runwal, G., Stamatakou, E., Siddiqi, F. H., Puri, C., Zhu, Y., and Rubinsztein, D. C. (2019) LC3-positive structures are prominent in autophagy-deficient cells. *Sci. Rep.* **9**, 10147
67. Schoof, M., Boone, M., Wang, L., Lawrence, R., Frost, A., and Walter, P. (2021) eIF2B conformation and assembly state regulate the integrated stress response. *eLife* **10**, e65703
68. Adomavicius, T., Guaita, M., Zhou, Y., Jennings, M. D., Latif, Z., Roseman, A. M., *et al.* (2019) The structural basis of translational control by eIF2 phosphorylation. *Nat. Commun.* **10**, 2136
69. Gordiyenko, Y., Llácer, J. L., and Ramakrishnan, V. (2019) Structural basis for the inhibition of translation through eIF2α phosphorylation. *Nat. Commun.* **10**, 2640
70. Murphy, M., James, Czabotar, E., Peter, Hildebrand, M., Joanne, Lucet, S., Isabelle, Zhang, J.-G., Alvarez-Diaz, S., *et al.* (2013) The pseudokinase MLKL mediates necroptosis *via* a molecular switch mechanism. *Immunity* **39**, 443–453
71. Meggio, F., Deana, A. D., Ruzzene, M., Brunati, A. M., Cesaro, L., Guerra, B., *et al.* (1995) Different susceptibility of protein kinases to staurosporine inhibition. Kinetic studies and molecular bases for the resistance of protein kinase CK2. *Eur. J. Biochem.* **234**, 317–322
72. Smith, I. M., and Hoshi, N. (2011) ATP competitive protein kinase C inhibitors demonstrate distinct state-dependent inhibition. *PLoS One* **6**, e26338
73. Glassman, F. Y., Schneider, J. L., Ramakrishnan, R., Dingman, R. K., Ramanathan, M., Bankert, R. B., *et al.* (2018) Phosphatidylserine is not just a cleanup crew but also a well-meaning teacher. *J. Pharm. Sci.* **107**, 2048–2054
74. Schneider, J. L., and Balu-Iyer, S. V. (2016) Phosphatidylserine converts immunogenic recombinant human acid alpha-glucosidase to a tolerogenic form in a mouse model of pompe disease. *J. Pharm. Sci.* **105**, 3097–3104
75. Sukkurwala, A. Q., Adjemian, S., Senovilla, L., Michaud, M., Spaggiari, S., Vacchelli, E., *et al.* (2014) Screening of novel immunogenic cell death inducers within the NCI mechanistic diversity Set. *OncoImmunology* **3**, e28473
76. Martins, I., Wang, Y., Michaud, M., Ma, Y., Sukkurwala, A. Q., Shen, S., *et al.* (2014) Molecular mechanisms of ATP secretion during immunogenic cell death. *Cell Death Differ.* **21**, 79–91
77. Kotecha, N., Krutzik, P. O., and Irish, J. M. (2010) Web-based analysis and publication of flow cytometry experiments. *Curr. Protoc. Cytom.* **53**, 10, 17.11-10.17.12